8.6 EXPANDING THE NOAA PROFILER NETWORK: TECHNOLOGY EVALUATION AND NEW APPLICATIONS FOR THE COASTAL ENVIRONMENT

A. B. White*[1,2], F. M. Ralph[2], J. R. Jordan[2], C. W. King[2], D. J. Gottas[1,2], P.J. Neiman[2], L. Bianco[1,2], and D. E. White[1,2]

[1]Cooperative Institute for Research in Environmental Sciences, University of Colorado, Boulder, CO
[2]NOAA Earth System Research Laboratory, Boulder, CO

1. INTRODUCTION

NOAA's costal and marine weather prediction suffers from a lack of in situ observations. In addition many satellite algorithms fail at the coast because of the interface between the continent and the oceans. This operational gap in NOAA's observing system motivated OAR's Earth System Research Laboratory (ESRL) to conduct an evaluation of two current, state-of-the art wind profiler technologies to determine which technology is better suited to marine and coastal weather applications.

Today, wind profilers are a mature technology used throughout the world (Fig. 1). NOAA Research and industry partners established a demonstration network of wind profilers in the central U.S. during the early 1990's (Fig. 2). This network is now referred to as the NOAA Profiler Network (NPN). A Cost of Operational Effectiveness Analysis (COEA) mandated by the U.S. Senate (108th Congress) was completed in 2004 to compare the "cost to upgrade the NOAA Profiler Network (NPN) over the next decade versus the short, medium, and longterm costs of ending the NPN program." The COEA concluded that "the best combination of performance and cost is to maintain the NPN system and modify its frequency so as not to interfere with reception by SARSAT satellites of signals from Search and Rescue beacons." Furthermore, the COEA added that "while other systems have individual attributes that may exceed the capability provided by NPN, there are significant physical or cost impediments that preclude their use in lieu of NPN." Partly in response to the COEA and to other well-documented results demonstrating the impact of the NPN data on forecast improvements, NOAA operationalized the NPN in 2005.

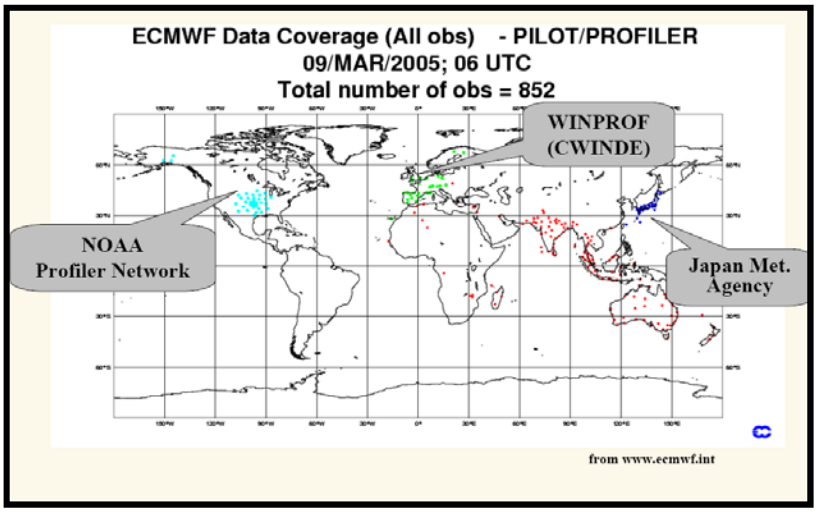

Figure 1. Worldwide wind profiler networks that provide data for model assimilation through the Global Telecommunication System (GTS).

* *Corresponding author address:* Allen B. White, NOAA/ESRL, R/PSD-2, 325 Broadway, Boulder, CO 80305; e-mail: allen.b.white@noaa.gov.

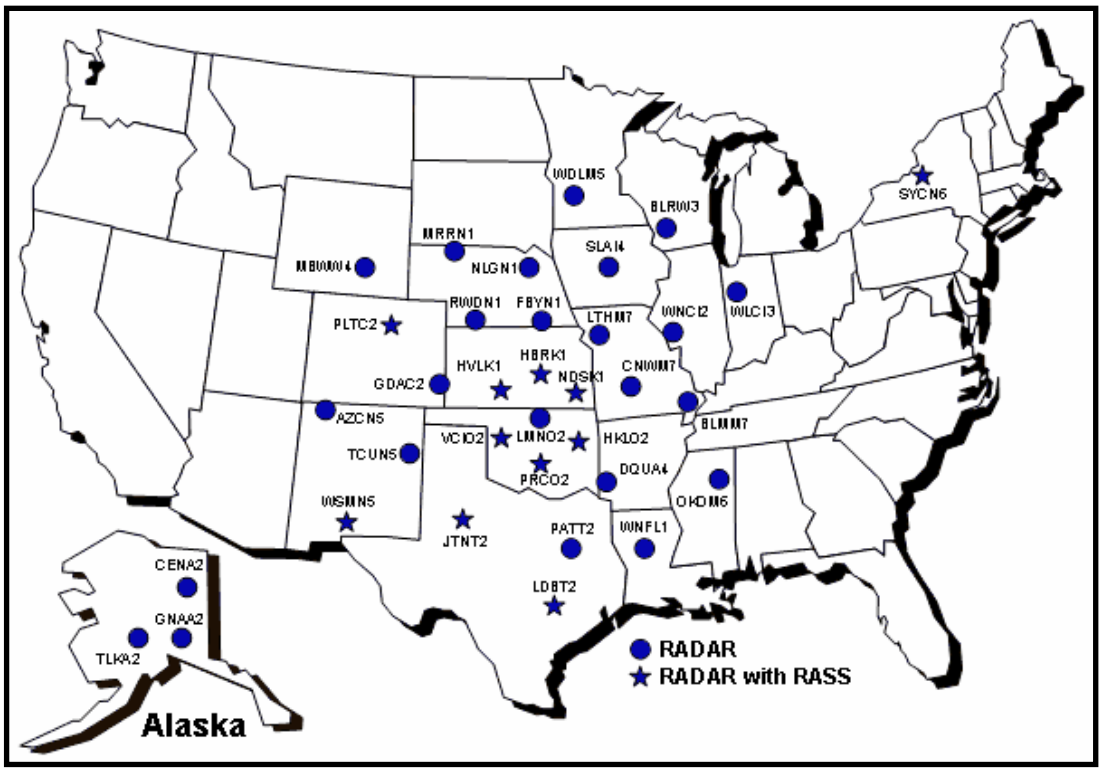

Figure 2. Map of the conterminous U.S. plus Alaska showing the locations of the NOAA Profiler Network (NPN). Sites instrumented with a wind profiler are indicated by circles. Sites instrumented with a wind profiler and a radio acoustic sound system (RASS) for temperature profiling are indicated by stars.

Figure 2 clearly indicates that none of the current NPN profilers is located in a coastal region. This is significant for the following reasons:

- Over 50% of the U.S. population lives in coastal areas that account for less than 20% of the nation's land, and coastal development still is increasing. 25% of the coast will be developed by 2025, versus 14% in 1997. As a result, more homes, businesses and lives will be vulnerable to coastal storms and more accurate forecasts will be required to reduce risks associated with hazardous weather.
- Approximately 50% of the 220 marine zones for which the NWS issues forecasts have no in-situ observations.
- Coastal storms account for 71% ($7B) of U.S. disaster losses. Coastal profiler networks would aid in reducing these losses by providing the NWS with the measurements necessary for improving short-term wind, precipitation, and aviation forecasts, including watches and warnings.

The NPN was originally designed to address forecast problems associated with convection and severe weather on the Plains. Deep vertical coverage was an important design requirement for the profiler technology used in the NPN in order to observe the deep convection that occurs in this region. However, most atmospheric processes and the variables associated with them observed in the coastal environment are shallow in nature, e.g., marine fog, marine stratus, marine-layer depth, marine-layer advection, continental outflow through breaks in terrain, downslope winds, low-level jets, and the melting layer. To help detect and monitor these features, a wind profiler that can observe close to the ground and upward with fine vertical resolution is required. These design attributes are in conflict with the current technology used in the NPN, although in 2007 NOAA was evaluating how to upgrade the NPN, based primarily on a mandate by the National Telecommunications and Information Administration (NTIA) to change the profiler operating frequency from 404 MHz to 449 MHz.

2. METHODOLOGY

The evaluation took place at the Bodega Bay Marine Laboratory north of San Francisco, California (BBY), and at the Santa Barbara Airport in Goleta, California (GLA), from September 2005 to August 2006. Two wind profiler technologies were evaluated: a 915-MHz boundary-layer wind profiler and a ¼-scale 449-MHz wind profiler. The 915-MHz wind profiler is small, easily transportable, commercially available, and has a proven track record in coastal weather and air quality applications. The more recently developed ¼-scale 449-MHz profiler is more expensive, commercially available, and a network of these radars recently has been installed along the Southern U.S. border and in Puerto Rico (Fig. 3). In addition to the wind profiler, ESRL operated a radio acoustic sounding system (RASS) for temperature profiling at each of the evaluation sites. However, because simultaneous RASS measurements at the two profiler operating frequencies could not be obtained at a single site because of interference issues, 915-MHz RASS data collected previously at GLA from September 2001 to August 2002 were used to compare with 449-MHz RASS data collected during the evaluation. Figures 4 and 5 identify the locations of the evaluation sites and illustrate the wind profiler and RASS equipment used at each site.

Each profiler technology was evaluated based on its operating performance (e.g., minimum and maximum altitude coverage) and its ability to detect and monitor key coastal weather phenomena. Other topics we addressed included operation and maintenance issues, and frequency security.

3. WIND PROFILERS

Wind profilers are Doppler radars that operate most often in the VHF (30-300 MHz) or VHF (300-1000 MHz) frequency bands. Three primary types of wind profilers were in operation in the U.S. at the time of this publication. The NOAA Profiler Network (NPN) profilers are fixed radars that operate at a frequency of 404 MHz (Chadwick, 1988). A smaller, transportable, commercially available wind profiler used by NOAA research and other agencies is the 915-MHz boundary layer wind profiler (Carter et al. 1995). The 404-MHz profilers provide the deepest coverage of the atmosphere, but lack coverage in the planetary boundary layer (PBL). The 915-MHz profilers provide the best coverage of winds in the PBL, but they lack height coverage much above the PBL. A third type of wind profiler that operates at 449 MHz combines the best sampling attributes of the other two systems. The physical, operating, and sampling characteristics of these wind profilers are listed in Table 1.

Wind profilers transmit pulses of electromagnetic radiation vertically and in at least two slightly off-vertical (~75 degree elevation) directions in order to resolve the three-dimensional vector wind. A small amount of the energy transmitted in each direction is reflected or backscattered to the radar. The backscatter returns are Doppler shifted by the motion of the scattering media. Profilers receive backscatter returns from atmospheric features (turbulence, clouds, precipitation) and non-atmospheric features (insects, birds, trees, airplanes, radio frequency interference). The challenge in signal processing is to avoid the returns from non-atmospheric scattering targets and focus on the atmospheric returns. To do this, profilers sample thousands of consecutive transmitted pulses to boost the signal-to-noise ratio of the atmospheric returns, a process known as coherent integration.

The return signals are sampled at discrete intervals called range gates. The size of the range gates is often equivalent to the length of the transmitted pulse, which is on the order of hundreds to thousands of nanoseconds (ns). For example, a 700 ns pulse translates into a non-oversampled range resolution of 105 m. Once the range-gated Doppler shifts from a set of beams have been determined, a wind profile is calculated. This process usually occurs over an observing period of 30 to 90 s. The wind profiles measured within a specified averaging period (15 min to 60 min) are averaged together using a consensus routine. The consensus routine filters outliers using threshold and acceptance windows. The consensus wind profiles are archived on site and transmitted back to a data hub in Boulder, Colorado via phone lines or, in remote areas, via satellite communications.

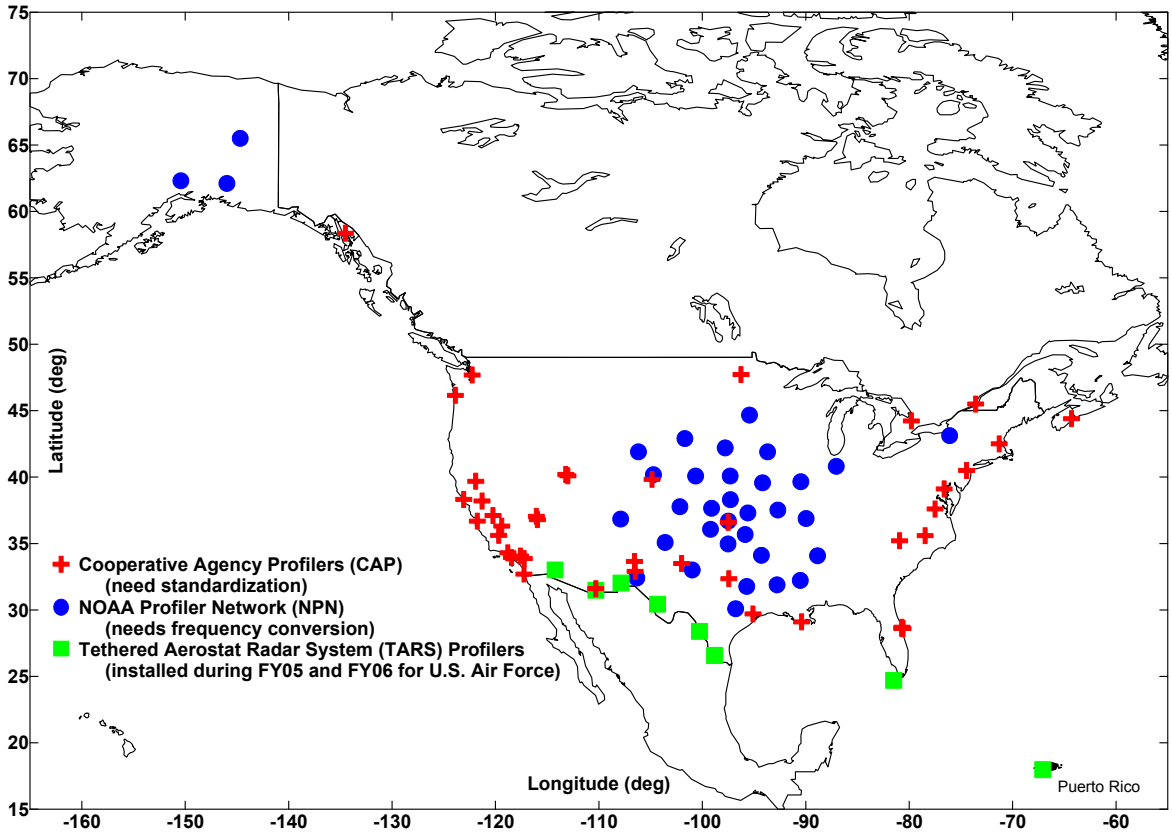

Figure 3. Map showing the locations of various U.S. and Canadian wind profiler networks. The locations of the recently installed TARS wind profilers are indicated by the green squares.

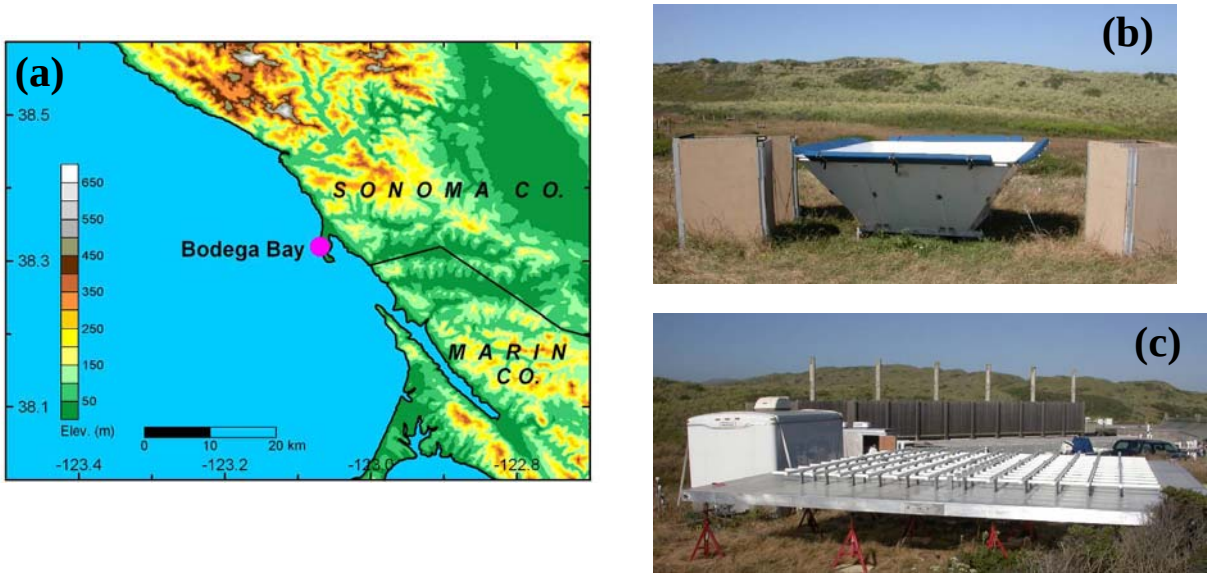

Figure 4. (a) Map showing the location of the Bodega Bay Marine Laboratory (BBY), where the primary technology evaluation took place. The (b) 915-MHz wind profiler with RASS and (c) ¼-scale 449-MHz wind profiler installed at BBY.

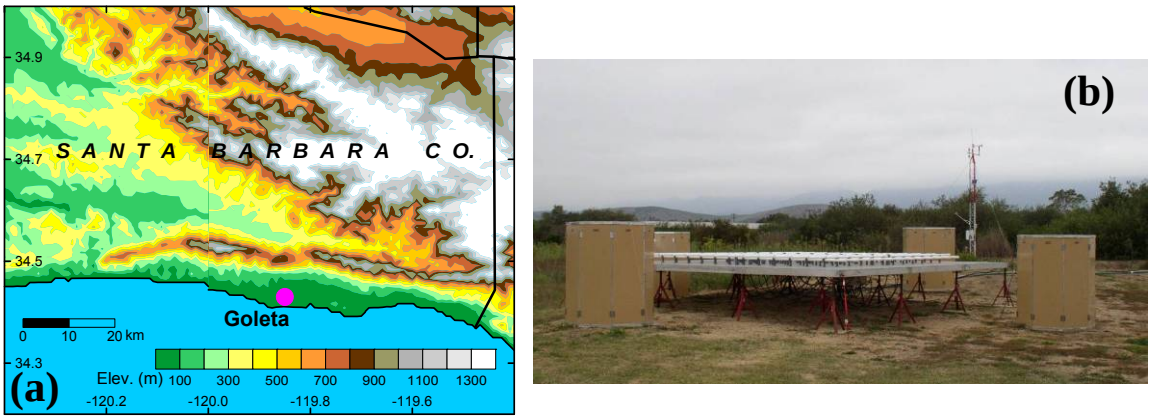

Figure 5. (a) Map showing the location of the Santa Barbra Airport in Goleta (GLA), where data from a RASS operating in conjunction with a 449-MHz profiler was collected. (b) The ¼-scale 449-MHz wind profiler with RASS installed at GLA.

Table 1. Physical, operating, and sampling characteristics of primary wind profiler technologies used in the U.S.

	915-MHz (boundary layer)	**449-MHz (quarter- scale)**	**404-MHz (NPN)**
Antenna type	Flat rectangular microstrip patch	Coaxial-colinear phased array	Coaxial-colinear phased array
Antenna diameter (m)	2	6	13
Beamwidth (deg.)	10	10	4
Peak transmit power (W)	500	2000	6000
Transmit pulse width (μs)	0.417*, 0.708*,p	0.708*, 2.833	3.3p, 20p
Height coverage (m)	120 – 4,000	180+ – 8,000	500** – 16,000
Vertical resolution (m)	63, 106*	106, 212*,♆	320♆, 900♆
Temporal resolution (min)	60	60	60

* These settings reflect how the profilers were operated during the IOOS technology evaluation. Other degraded transmit and sampling resolutions are possible.

p Pulse-coding was used in selected operating modes to boost signal power and increase altitude coverage (for more information on pulse coding, see Ghebrebrhan, 1990).

\+ This minimum detectable range has been achieved with the ¼-scale 449-MHz profilers using a 0.7-μs pulse.

** Signal attenuators prevent accurate radar reflectivity data below 1 km.

♆ Increased vertical resolution as compared to the transmit pulse length was accomplished by oversampling.

Certain parts of the analyses presented in Section 4 used the wind profiler data collected in real time during the evaluation in order to represent the actual data that would have been available to forecasters in near-real time. Other parts of the analyses in Section 4 used wind data that were post-processed after the evaluation with the NOAA wind profiler quality control algorithms. Following is a brief description of the process used to quality control wind profiler data.

Although traditional signal-processing methods are designed to remove unwanted non-atmospheric signals from the Doppler spectrum, there are still contaminated spectral signals that produce erroneous moment-level data and, subsequently, wind profiles. Quality control algorithms are implemented to identify and remove

these erroneous data that would otherwise render inaccurate meteorological measurements and interpretation. ESRL currently uses a continuity method developed by Weber et al. (1993) to identify and preserve only those measurements that exhibit consistency in height and time.

The continuity method is based on the fundamental assumption that some valid data are present in the comparison domain. The degree of continuity of an individual data point is established by comparing its data value with the value interpolated from neighboring data points. A data value is considered discontinuous with its neighbors if the comparison exceeds a prescribed threshold. The size of the domain used in the interpolation typically consists of two neighboring heights above and below and two neighboring times before and after. A linear least-squares interpolation is used to increase the tolerance for large slopes in the data. Therefore, meteorological features of interest, such as shears and accelerations in the wind field and temperature gradients in the vicinity of fronts, are determined to be continuous.

Because erroneous measurements can also exist in the form of continuous time-height clusters, the point-continuity test can fail to identify erroneous data values at individual data points whose comparison domains lie completely within the erroneous cluster. To combat this potential problem, the continuity algorithm uses pattern recognition to identify erroneous data clusters. Patterns in a data set are formed by identifying subsets of data that are continuously connected. Neighboring points with similar values are placed in the same branch of some pattern. Additional branches are identified when neighboring points have different values. These branches may be part of the same pattern or may belong to completely different patterns. After all of the patterns in the data set have been recognized, a series of continuity tests are performed to identify discontinuities between the different branches while attempting to preserve the largest pattern size.

These methods have produced high quality results under a variety of meteorological conditions over many months of observations. Nevertheless, certain types of contamination, such as ground and sea clutter, can persist over time with consistent Doppler shift over many heights. In these situations, the continuity method can produce undesirable results. Perhaps the combined use of the continuity method with newly developed signal-processing techniques, such as the multiple peak-picking algorithm (Wolfe et al., 2001), will provide the higher levels of intelligence needed to remove even the severest types of spectral contamination.

4. RESULTS

4.1 *Wind Profile Altitude Coverage*

All data used in this section were processed using the NOAA wind profiler quality control algorithms described in Section 3. The wind datasets also were inspected visually to remove migrating bird contamination (Wilczak et al., 1995). Data passing both the quality control algorithms and the visual inspections are referred to as valid data points. The altitude coverage analyses considered the entire evaluation period as well as seasonal periods for the fall (September through November), winter (December through February), spring (March through May), and summer (June through August). Using the processed hourly-averaged wind profiler wind data and RASS virtual temperature data, ensemble-averaged datasets were created separately for the 11-month period and the four seasonal periods. Valid data points in the final datasets represent winds or temperatures where 50% or greater of the available hourly-averaged data were valid. Maximum height coverage represents the level above which less than 50% of the averaged data points were valid. Each profiler operated in two operating modes for winds and a single operating mode for RASS. For winds, the finer vertical resolution mode (63 m for the 915-MHz wind profiler and 106 m for the 449-MHz wind profiler) is referred to as the “low mode,” owing to the lower maximum altitude that can be achieved using a shorter transmitted pulse, and the coarser vertical resolution mode (106 m for the 915-MHz wind profiler and 212 m for the 449-MHz wind profiler) is referred to as the “high mode.”

Results of the altitude coverage analyses are summarized in Table 2 for winds and Table 3 for RASS temperature profiles. Diurnal composites produced from the ensemble-averaged datasets are shown in Fig. 6 for winds and Fig. 7 for RASS. For winds, the lowest range gate on the 915-MHz wind profiler high mode was 110 m above ground. This range gate provided reliable, quality-controlled wind data 95-98% of the time. The lowest range gate on the 449-MHz wind profiler low mode was 185 m above ground. This range

gate provided reliable, quality-controlled wind data 90-95% of the time. The reduced performance of the 449-MHz wind profiler's lowest range gate is likely due to a problem with the radar's receiver that was corrected only a few weeks into the study. The lowest range gate on the 915-MHz RASS is 135 m above ground compared to 217 m above ground for the 449-MHz RASS. For winds, the difference in minimum altitude coverage is 75 m, and for RASS, the difference is 82 m.

Using pulse coding and a 2.8 μs transmitted pulse (high mode), the BBY 449-MHz wind profiler achieved more than three times the maximum altitude coverage (6845 m vs. 2243 m above sea level) of the BBY 915-MHz wind profiler using pulse coding and a 0.7 μs pulse (high mode). The 449-MHz RASS at GLA outperformed the 915-MHz RASS at GLA in maximum altitude coverage by nearly 700 m (1734 m vs. 1047 m above sea level). In addition, the 449-MHz wind profiler at BBY provided reliable, quality-controlled data up to 5000 m above sea level 90% of the time. The 915-MHz wind profiler at BBY provided reliable, quality-controlled data up to 1400 m above sea level 90% of the time. The ability of the 449-MHz wind profiler to obtain more reliable altitude coverage above the planetary boundary layer is due to its longer operating wavelength and an increased sensitivity to clear-air turbulence.

Although no quantitative results are available to show which wind profiler or RASS provided the better overall data quality, the overwhelming impression given by the engineers and radar scientists who worked on this project is that the Doppler spectra from which the winds and RASS temperatures are estimated are much cleaner for the 449-MHz wind profiler than for the 915-MHz profiler. This makes the job of signal processing much easier and should produce a more robust product. A difference in data quality was most noticed in the observed temperature profiles from RASS, where the 449-MHz system produced much cleaner, less noisy profiles than the 915-MHz RASS.

Table 2. Bodega Bay (BBY) 449-MHz and 915-MHz wind profiler maximum altitude coverage statistics.

	Fall	*Winter*	*Spring*	*Summer*	*All data*
449-MHz high mode					
Mean height (m)	7111	6734	6760	6922	6845
915-MHz high mode					
Mean height (m)	2229	2120	2369	2255	2243
Difference (m)	4882	4614	4391	4667	4602

Table 3. Goleta (GLA) 449-MHz and 915-MHz RASS virtual temperature maximum altitude coverage statistics.

	Fall	*Winter*	*Spring*	*Summer*	*All data*
449-MHz RASS					
Mean height (m)	1703	1585	1809	1991	1734
915-MHz RASS					
Mean height (m)	955	937	1128	1157	1047
Difference (m)	748	648	681	834	687

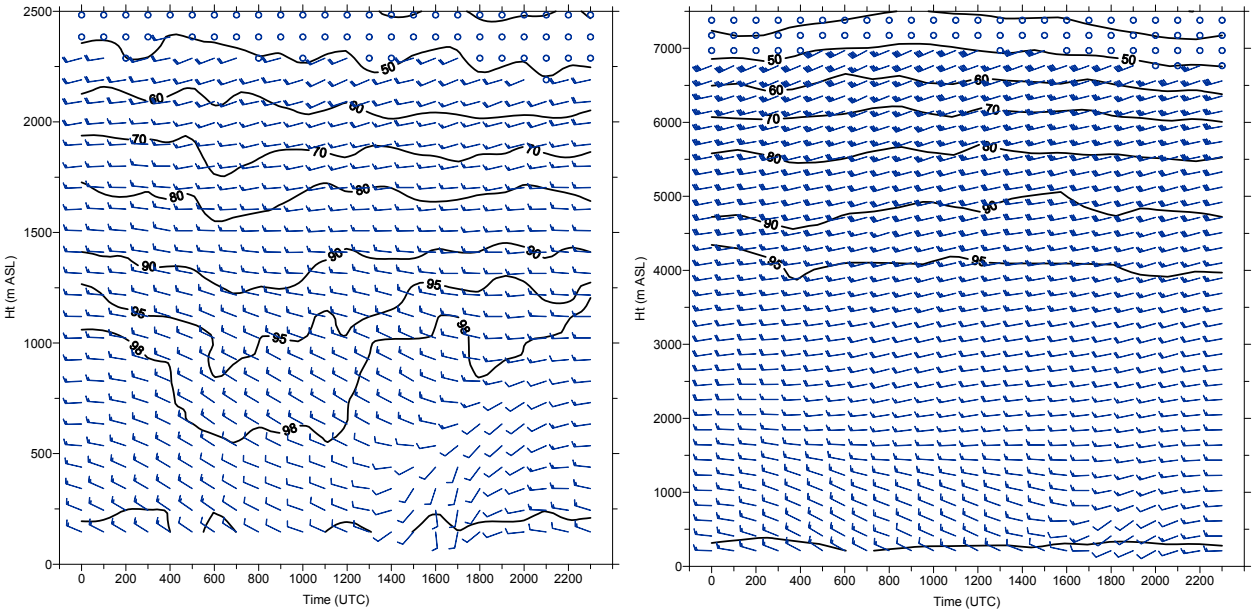

Figure 6. Diurnal composites of wind profiles measured by the Bodega Bay (BBY) 915-MHz wind profiler (left and 449-MHz wind profiler (right) during the 11-month technology evaluation period (September 15, 2005-August 15, 2006). Wind barb convention: a full barb is 5 m s^{-1} and a half barb is 2.5 m s^{-1}. Contours indicate the percentage of valid data points used to obtain the composites.

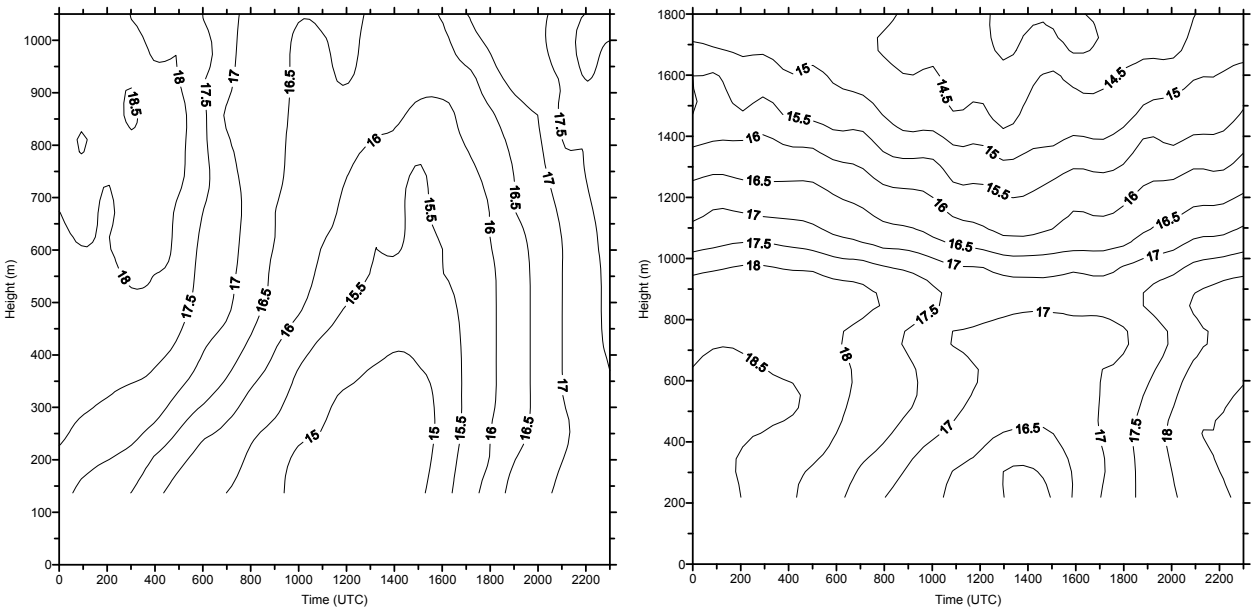

Figure 7. Diurnal composites of virtual temperature profiles measured by the GLA 915-MHz RASS (left) during the 11-month period (September 15, 2001-August 2002) and by the GLA 449-MHz RASS (right) during the corresponding technology evaluation period (September 15, 2005-Augutst 15, 2006).

4.2 *Gap Flow*

During winter, channeled air streams regularly exit California's Central Valley to the coast through its only major airshed outlet, the Petaluma Gap (Fig. 8; from Neiman et al., 2006). These wintertime gap flows are generally less pronounced than those observed farther north [i.e., in the Pacific Northwest (e.g., Colle and Mass, 2000; Sharp, 2002), British Columbia (e.g., Mass et al., 1995; Jackson and Steyn, 1994), and Alaska (e.g., Bond and Stabeno, 1998; Loescher et al., 2006; Colman and Dierking, 1992)], in part because the Petaluma Gap is poorly defined by comparison (~35-50 km wide, and walls extending a modest 600-900 m above the valley floor – see Fig. 8b). Petaluma Gap flows are also weaker because the source of cold air is California's Central Valley rather than the northern interior of North America where arctic air is ubiquitous. Specifically, the Sierra Nevada Mountains act as a continuous 3-4 km tall barrier that prevents very cold air in the continent's interior from regularly entering the Central Valley. Rather, cold air in the Central Valley usually forms in-situ when air within the valley stagnates beneath a capping subsidence inversion and radiatively cools for an extended period of time, often producing widespread fog or stratus which inhibits diurnal heating (e.g., Gilliam, 1970; Holets and Swanson, 1981; Underwood et al., 2004). Nocturnal katabatic flows from the Sierras can also contribute to the generation and maintenance of the cold pool.

Despite the comparatively weak character of flows though the Petaluma Gap relative to their northern counterparts, these flows can significantly impact the local distributions of wind, temperature, precipitation, and atmospheric pollutants along the coast, as has been documented in detail in a five-winter wind profiler study by Neiman et al. (2006). Channeled flows exiting the Petaluma Gap preferentially occur in pre-cold-frontal conditions, largely because sea-level pressure decreases westward along the gap in a stably stratified atmosphere in advance of approaching cold-frontal pressure troughs. These flows are only several hundred meters deep and characterized by relatively cold, easterly flow capped by a layer of enhanced static stability and directional vertical wind shear. They can contribute to coastally trapped air streams in California, as has also been found in the coastal zone of Alaska by Loescher et al. (2006) and Colle et al. (2006).

Given the importance of channeled flows exiting the Petaluma Gap to regional weather, we deemed it instructive to take advantage of this shallow, terrain-anchored phenomenon to explore the capabilities and limitations of the ¼-scale 449-MHz wind profiler at BBY during the winter of 2005-2006. The basic analysis methodology employed for this study was the same as that in Neiman et al. (2006). Namely, we defined gap-flow events based on quality-controlled 915-MHz wind profiler data and surface observations at BBY meeting the following criteria for at least six consecutive hours: (1) a surface wind direction of 50-120 degrees, (2) a layer-mean wind direction of 60-130 degrees between 100-350 m MSL (i.e., in the lowest three profiler range gates), and (3) an easterly component of at least 5 m s-1 in the same 100-350 m layer. A total of 19 gap-flow events were observed between November 1, 2005 and April 26, 2006 (Table 4).

The 19 gap-flow events (Table 4) ranged between 6 and 41 h in duration, with a mean time interval of ~14 h. Each case exhibited an above-surface maximum of low-level easterly-component flow (hereinafter referred to as a gap jet) beneath the top of the gap walls, with the mean altitude of this maximum residing at 306 m MSL. The mean magnitude of the gap jet was 8.9 m s-1 and was bounded by cases as strong as 13.1 m s^{-1} and as weak as 6.0 m s^{-1}. Most of the 19 cases were rain-free at both BBY and the nearby mountain site at CZD (situated at 475 m MSL), thus supporting the conclusions drawn from the 5-winter study by Neiman et al. (2006) that gap-flow events inhibit rainfall near its exit at the coast. In addition, without exception, the summary gap-flow statistics based on the analysis of the 2005-2006 profiler data mirror those of the 5-winter study. Hence, the gap flow characteristics observed at BBY during the winter of 2005-2006 should be deemed representative.

The mean vertical structure of the flow through (and above) the Petaluma Gap was evaluated by averaging all 270 hourly, quality-controlled wind profiles from the 19 gap flow cases into composite profiles of total wind speed, wind direction, and zonal and meridional wind components (dark blue curves in Fig. 9a-d). The number of data points available at each range gate (a maximum of 270 for the winter of 2005-2006 versus 937 for the five-winter study) is shown in Figs. 9e,f. The composite wind speed and direction profiles portray a gap jet (9.5 + 2.5 m s^{-1}) directed from the east-southeast (i.e., from the Petaluma Gap)

centered on the third range gate (i.e., at ~300 m MSL). The magnitude of the flow decreases significantly across a prominent directional shear layer at ~0.5 km MSL and remains weaker than the gap jet upward through 2 km MSL. Clockwise turning of winds with height from southeasterly to southerly above the gap flow suggests the presence of pre-cold-frontal warm advection, consistent with the findings in Neiman et al. (2006). Inspection of the composite zonal wind profile reveals a well-defined easterly gap-jet signature (9.2 + 2.3 m s^{-1}), also at the third range gate. In contrast, the meridional wind profile shows a steady increase with height of the magnitude of the southerly component flow (from nearly zero to more than 8 m s^{-1}) in the lowest 1.5 km MSL. These composite profiles are remarkably similar to those based on the five-winter study (dashed curves in Figs. 9a-d), although the altitude of the gap jet was slightly higher (by less than 100 m) during the winter of 2005-2006. These composite profiles also mirror their counterparts derived from the real-time 915- and 449-MHz profiler data during the winter of 2005-2006 (light blue and yellow curves in Figs. 9a-d), with the notable exception that the gap jet resided in the two lowest range gates of the 449-MHz profiler (i.e., at ~200-300 m MSL).

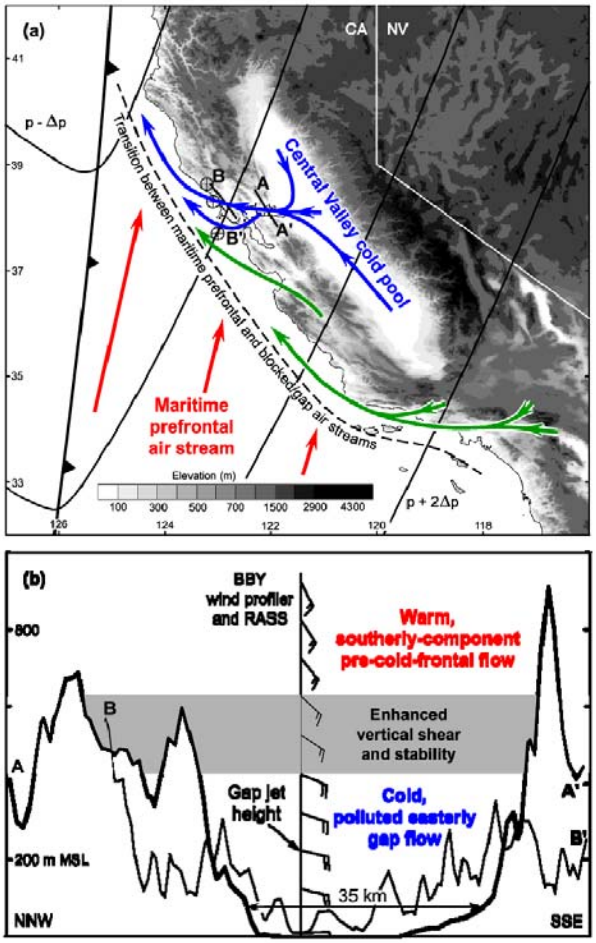

Figure 8. (a) Plan view conceptual representation of cold, dry gap flow at the surface originating from California's Central Valley (solid blue) and exiting the Petaluma Gap near the BBY profiler (the middle circular symbol along the coast) and the Golden Gate Gap near San Francisco. Gap flow is also shown exiting the interior farther to the south (green lines). A warm maritime prefrontal air stream is portrayed (red) ahead of an advancing cold front. Solid black lines are isobars, and the dashed black line marks the transition between the prefrontal and blocked/gap air streams. Bold lines AA' and BB' are cross-section projections across the Petaluma Gap in (b). Terrain is shaded (see key). (b) Schematic terrain cross sections along AA' and BB' highlighting the key kinematic and thermodynamic attributes of shallow, easterly flow through the Petaluma Gap, based on composite wind profiles from BBY (barbs = 5 m s^{-1}; half-barbs = 2.5 m s^{-1}) and collocated RASS observations. From Neiman et al. (2006)

Table 4. Gap-flow case inventory (19 total) and gap jet characteristics based on quality-controlled 915-MHz wind profiler data at BBY between 1 Nov 2005 and 26 Apr 2006. Rainfall at BBY and CZD are also shown. Summary statistics from the five-winter gap flow wind profiler study between November 1997 and March 2004 by Neiman et al. (2006) are provided at the bottom.

Start date/time	Hours	Gap flow jet. Altitude of max. easterly flow (m, MSL)	Gap flow jet. Magnitude of max. easterly flow ($m\ s^{-1}$)	Gap flow jet. Wind dir. in max. easterly flow (deg)	Rainfall at BBY (mm)	Rainfall at CZD (mm)	Rainrate at BBY ($mm\ h^{-1}$)	Rainrate at CZD ($mm\ h^{-1}$)
16Nov05 08Z	12	512	9.0	93.3	0.0	0.0	0.0	0.0
18Nov05 13Z	9	317	9.2	86.3	0.0	0.0	0.0	0.0
28Nov05 21Z	9	221	9.0	115.4	19.558	23.622	2.173	2.625
30Nov05 15Z	11	221	7.7	108.4	0.0	0.508	0.0	0.046
07Dec05 22Z	17	317	7.5	102.5	0.508	0.254	0.030	.015
18Dec05 02Z	9	317	13.1	121.3	35.052	25.908	3.895	2.879
24Dec05 00Z	24	317	9.2	103.0	0.254	0.254	0.011	0.011
04Jan06 12Z	6	221	7.9	111.1	0.508	0.254	0.085	0.042
04Jan06 22Z	41	221	10.3	106.3	0.0	0.0	0.0	0.0
13Jan06 03Z	17	221	9.2	108.9	0.0	0.0	0.0	0.0
24Jan06 16Z	10	317	8.4	99.0	0.0	0.0	0.0	0.0
06Feb06 06Z	34	317	9.7	94.5	0.0	0.0	0.0	0.0
09Feb06 07Z	17	317	10.4	88.1	0.0	0.0	0.0	0.0
19Feb06 05Z	8	512	8.2	77.8	0.0	0.0	0.0	0.0
15Mar06 05Z	6	317	6.0	127.2	0.508	0.0	0.085	0.0
21Mar06 12Z	6	317	7.8	104.0	0.0	0.0	0.0	0.0
02Apr06 15Z	14	342	8.5	120.2	12.700	11.430	0.907	0.816
04Apr06 10Z	11	244	10.3	103.4	3.556	4.572	0.323	0.416
12Apr06 18Z	9	244	8.1	109.5	2.286	3.048	0.254	0.339
Total	270				74.93	69.85		
Mean (all)	14.2	305.9	8.9	104.2	3.944	3.676	0.278	0.259
Standard Dev.	9.5	85.3	1.5	12.6	9.115	7.936	0.992	0.863
Minimum	6	221	6.0	77.8	0.0	0.0	0.0	0.0
Maximum	41	512	13.1	127.2	35.052	25.908	3.895	2.879
5-y study Total	937				57.404	103.632		
Mean (all)	15.1	226.4	9.1	104.8	0.926	1.919	0.061	0.120
Standard Dev.	13.3	113.0	1.9	14.5	2.567	4.894	0.216	0.307
Minimum	6.0	105.0	6.0	66.4	0.0	0.0	0.0	0.0
Maximum	73.0	741.0	16.2	139.1	10.668	25.652	1.334	1.588

4.3 *Melting Layer*

The melting layer is the vertical layer of the atmosphere in which frozen hydrometeors transform into liquid hydrometeors during precipitation. The presence and location of the melting layer serves as important information for weather forecasters, hydrologists, water-resource managers, and emergency managers to asses or address rain/snow levels, water-management operations, and flooding issues.

The use of wind profilers offers an innovative approach to continuously monitor the melting layer during precipitation events. The Rayleigh scattering process, which has a strong inverse dependence on the wavelength of radiation being scattered, allows wind profilers in the UHF frequency band to detect hydrometeors in addition to the atmospheric turbulence that provides backscatter for clear-air wind profiling. Hydrometeors existing within the melting layer further enhance the backscatter of radar energy, owing to the aggregation and water coating of snow flakes in the upper region of the layer and the mass flux divergence of rain drops in lower region of the layer (Batton, 1973). These processes within the melting layer produce enhanced reflectivity, as sensed by the radar, which is referred to as the radar bright band (hereafter referred to RBB). NOAA has been detecting the RBB in real-time on many of its remotely operated wind profilers since 2002 (White et al., 2002). These data have been visualized and made accessible to NWS forecasters and the public through web interfaces in near real time. An example of this product is shown in Fig. 10.

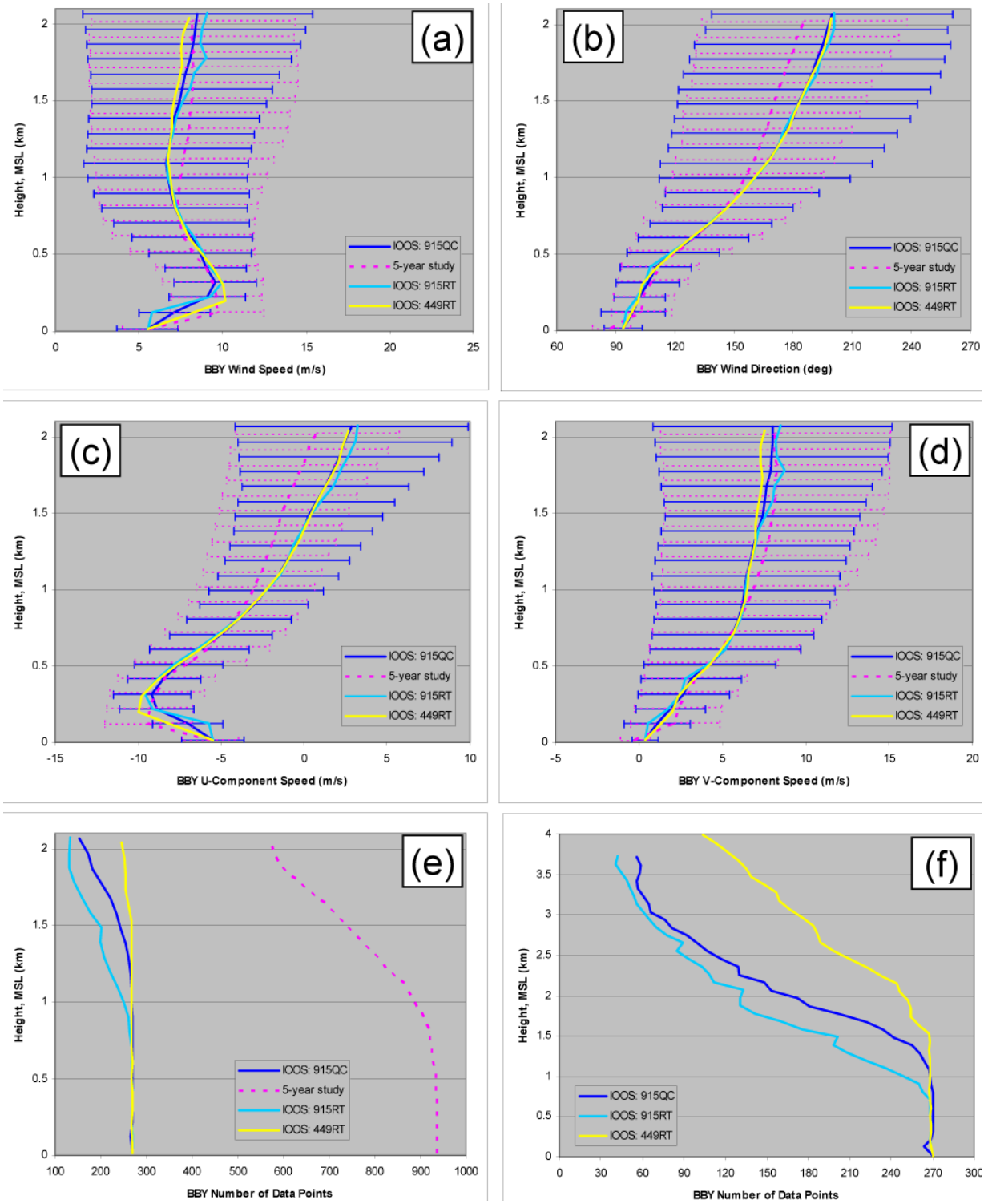

Figure 9. Composite mean profiles from the BBY wind profilers based on all 19 gap-flow cases observed during the winter of 2005-2006 (solid curves; dark blue = 915-MHz quality-controlled data, light blue = real-time 915-MHz data, yellow = real-time 449-MHz data). Composite mean profiles based on the 5-winter, 62-case study by Neiman et al. (2006) are also shown (dashed curves). (a) wind speed (m s^{-1}), (b) wind direction (deg), (c) U-component (i.e., zonal) wind speed (m s-1), (d) V-component (i.e., meridional) wind speed (m s^{-1}), (e) number of hourly points per range gate, and (f) number of hourly points per range gate up to 4 km MSL for the current datasets only.

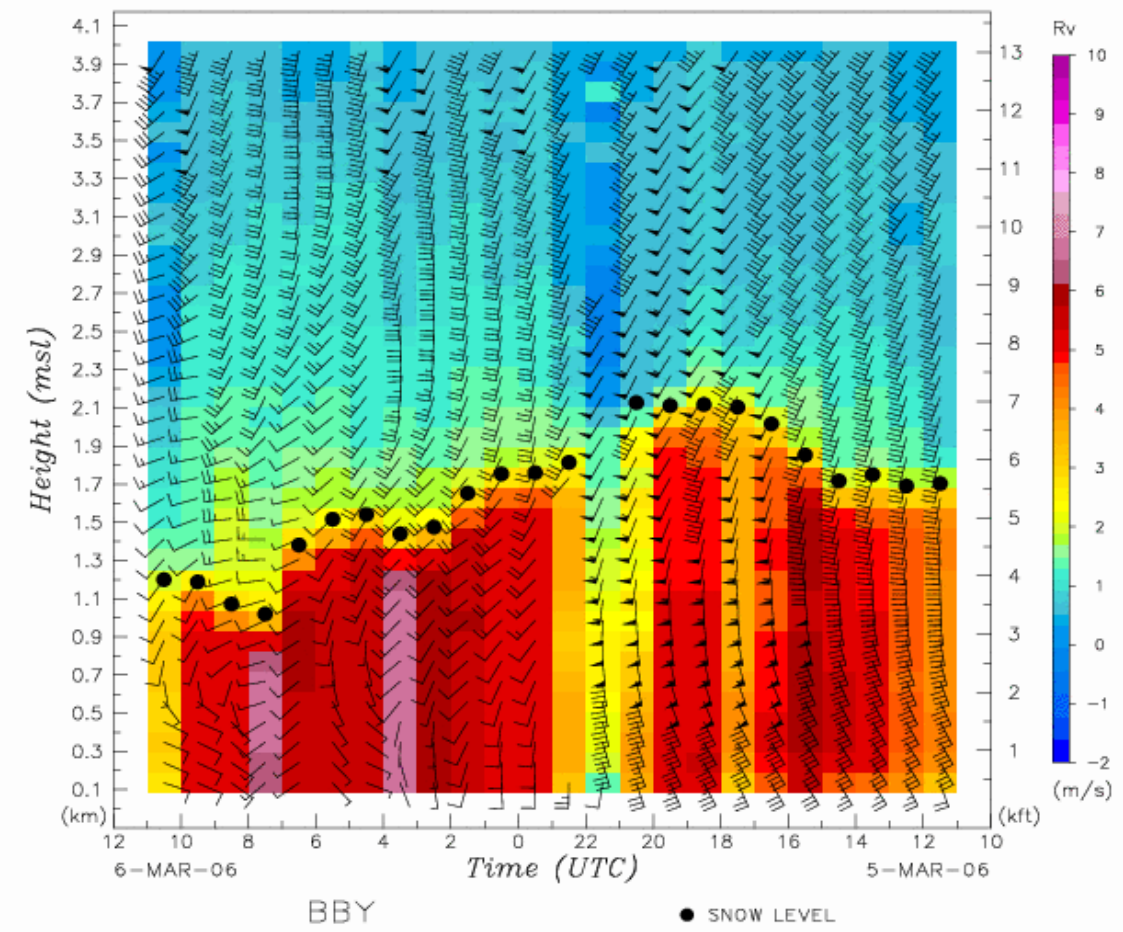

Time (UTC)	1030	0930	0830	0730	0630	0530	0430	0330	0230	0130	0030	2330
Snow Level (m)	1200	1188	1072	1020	1381	1516	1541	1440	1475	1653	1754	1760
Snow Level (ft)	3935	3896	3516	3345	4529	4972	5054	4723	4837	5421	5753	5772
Sfc Temp (C)	6.72	6.90	7.20	7.61	8.38	8.32	8.47	8.92	9.32	9.58	9.77	10.22

Time (UTC)	2230	2130	2030	1930	1830	1730	1630	1530	1430	1330	1230	1130
Snow Level (m)	1814	none	2127	2111	2117	2103	2016	1853	1717	1750	1690	1703
Snow Level (ft)	5949	none	6976	6924	6943	6897	6612	6077	5631	5739	5543	5585
Sfc Temp (C)	10.64	10.78	10.85	10.84	10.61	10.53	10.33	10.37	10.52	10.51	10.57	10.86

Figure 10. An example of NOAA's near-real-time, web-based, snow-level product (White et al., 2002) from the 915-MHz radar located at Bodega Bay, California (BBY), on March 5-6, 2006. The radar bright-band heights are represented by the black dots, and the hourly-averaged vertical radial velocity associated with the hydrometeor fall speeds is contoured in color. Time increases from right to left on the horizontal axis.

Both the 915-MHz and 449-MHz radar wind profilers are capable of detecting precipitation and the RBB. When considering radar wavelength alone, the shorter wavelength of the 915-MHz radar (33 cm) makes it more sensitive for detecting the RBB than the 449-MHz radar (67 cm). However, the 449-MHz radar uses a low-noise receiver and a larger antenna than the 915-MHz radar, which more than compensates for the sensitivity difference due to wavelength. The larger antenna allows for more scattered energy to be received by the radar, while the low-noise receiver produces signals with higher signal-to-noise ratios in the Doppler spectrum that are more

easily detected by signal-processing algorithms. As depicted in Fig. 11, the combined effect of these hardware features makes the 449-MHz radar more sensitive for detecting precipitation than the 915-MHz radar. However, because the 449- MHz radar is also able to detect much weaker levels of atmospheric turbulence than the 915-MHz radar (also shown in Fig. 4.2-2), there is a much greater likelihood for two signal peak regions to exist in the 449-MHz Doppler spectra during precipitation – one from hydrometeors and another from the atmosphere. This scenario poses an additional challenge for signal-processing algorithms to select the desired signal associated with the RBB.

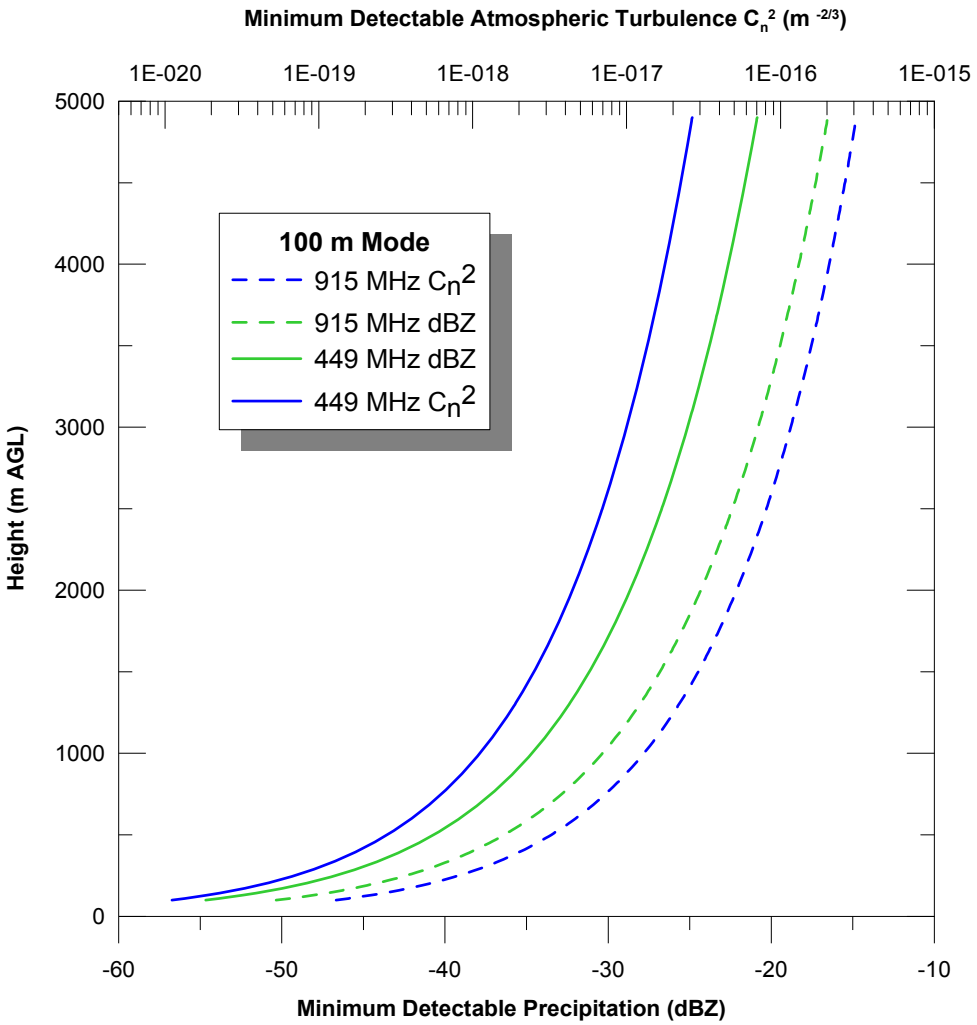

Figure 11. Vertical profiles of minimum detectable C_n^2 and dBZ for the wind profiler operating modes that used the 0.708-μs pulse width. The solid (dashed) lines correspond to the 449-MHz (915-MHz) collocated wind profiling radars.

Over the course of 66 days during the 218-day analysis period, a RBB was detected 322 times by both radars during identical hours. The relative accuracy for these matched data was high, with a correlation coefficient of ~ 0.9993. With respect to data retrieval, the 915- MHz radar detected 22% more RBBs than the 449-MHz radar, while the 449-MHz radar only detected 3% more RBBs than the 915-MHz radar. This result is contrary to what might be expected, when considering the effect of radar sensitivity to precipitation alone (see Fig. 11).

The improved data-retrieval performance of the 915-MHz radar is accounted for by two factors. First, as alluded to earlier, the utilization of both 915-MHz operating modes (i.e., the 60-m and 100-m modes) allows for more comprehensive temporal sampling during the hour, and also produces a more statistically robust result by increasing the sample population for the bright-band-detection algorithm. In addition, the higher vertical resolution of the 60-m mode provides a better approximation of the bulk gradients near and within the RBB. This is of particular importance for detecting RBBs that are shallow in depth or close to the earth's surface. This first factor accounts for 36% of the improved data-retrieval performance. The second and most prevalent factor results from the superior sensitivity of the 449-MHz radar for detecting clear-air echoes from atmospheric turbulence. This increased level of sensitivity allows signals from both the turbulence and precipitation to be resolved simultaneously in the 449-MHz Doppler spectrum. During light precipitation events, which correspond to lower values of radar reflectivity, the magnitude of the precipitation and turbulence echoes often can be nearly equivalent. This situation can pose a serious challenge for spectral-peak-picking algorithms to correctly and consistently identify precipitation signals for RBB detection. This was the case during several of the light and intermittent precipitation events encountered during the analysis period. It should be noted, however, that since the spectral-peak-picking logic was originally developed for 915-MHz Doppler radars, most of these 449-MHz dual-signal cases would likely be identified correctly with relatively minor enhancements to the algorithm.

Lastly, the impact of the additional data retrieved by the 915-MHz radar was assessed. This impact was formulated in two ways. First, to what degree did the additional data aid in identifying the RBB for individual precipitation events? And, second, what type of association did these additional RBB data have with the amount of precipitation received at the surface? This targeted assessment may help determine to what degree the additional data provide beneficial information to the end user, such as weather forecasters or water-resource managers. In addressing the first question, 77% of the additional 915-MHz RBBs occurred during precipitation events that had at least one other RBB detected by the 449-MHz radar. Of these samples, a 449-MHz RBB was detected within +/- 2 hours of the 915-MHz RBB 72% of the time, with the remaining percentage occurring within +/- 3 to 7 hours. The remaining 33% of the additional 915-MHz RBBs occurred without a neighboring 449-MHz RBB, and were all associated with intermittent precipitation events lasting 1 to 2 hours. The second question is addressed by reviewing the hourly accumulated precipitation, as acquired from a collocated surface rain gauge, during times when the additional RBBs were retrieved by the 915-MHz wind profiler. Figure 12 depicts the accumulated rainfall for all hours when a RBB was detected by both the 915-MHz and 449-MHz profilers (top panel), and for those hours when a RBB was only detected by the 915-MHz profiler (lower panel). The lower panel shows that most of the additional RBBs (97%) were associated with light precipitation regimes (accumulation less than or equal to 2 mm per hour). This result is consistent with the earlier explanation that the 449-MHz detection loss is associated with erroneously distinguishing light precipitation echoes from atmospheric turbulence echoes in the Doppler velocity spectrum. In addition, the hydrological consequences of excluding these additional RBBs, which are absent in the 449-MHz data set, are relatively low owing to their minimal contributions to rainfall runoff.

4.4 *Boundary-layer Depth*

In this section, the 449-MHz wind profiler data collected at BBY is referred to as BBY-449 and the 915-MHz wind profiler as BBY-915. For the Goleta site the 449-MHz wind profiler is referenced to simply as GLA. The analysis was performed for the time period from May 1st to August 14th (Julian days 121 to 226), 2006, for both sites.

For wind profiler estimations we relied on the information obtained by the behavior of signal-to-noise ratio (SNR), variance of vertical velocity, and Doppler spectral width. An automated algorithm was run through the period of interest and a visual inspection of the data was performed for every day to correct for possible algorithm inaccuracies. The visual inspection was performed on three-panel plots that illustrate the behaviour of range-corrected SNR, vertical velocity, and Doppler spectral width. For non-coastal sites the automated algorithm has been shown to provide accurate estimates of the depth of the turbulent, convective planetary boundary layer (Bianco and Wilczak, 2002; Bianco et al., 2007).

For RASS estimations we considered the virtual temperature, T_v, profile taken during the first 5 minutes of each hour to provide an hourly estimate of the boundary layer depth. We converted T_v to virtual potential temperature, θ_v, and determined the first point in the θ_v profile at which the value of the gradient of θ_v as a function of height is larger than an arbitrary threshold. This technique is used to estimate the height of the marine inversion. However, often the lapse rate is stably stratified below the marine inversion. This stable layer may be intermittently turbulent, or it may be a layer with primarily laminar flow.

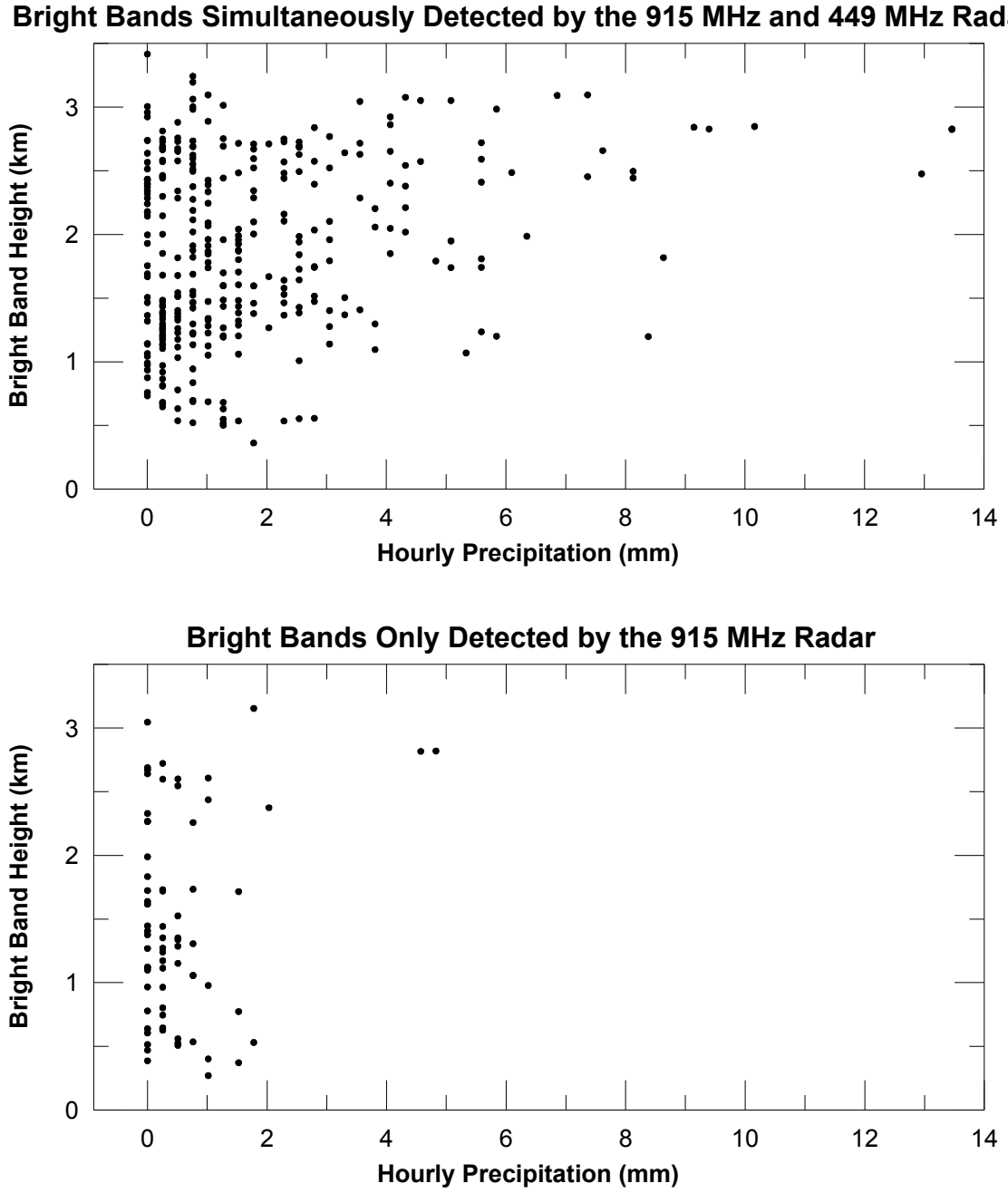

Figure 12, Hourly accumulated precipitation as a function of bright-band height for bright bands simultaneously detected by the 915-MHz and 449-MHz radars (top panel) and for bright bands only detected by the 915 MHz radar (bottom panel).

Figure 13 shows an example of BLD estimations calculated on Julian day 136 by the two wind profilers at BBY. Because the marine boundary-layer is often only a few hundred meters deep, the finest vertical resolution data collected by each wind profiler were used. For the BBY-915, this corresponds to 60-m vertical resolution, while for the BBY-449 this corresponds to 100-m vertical resolution.

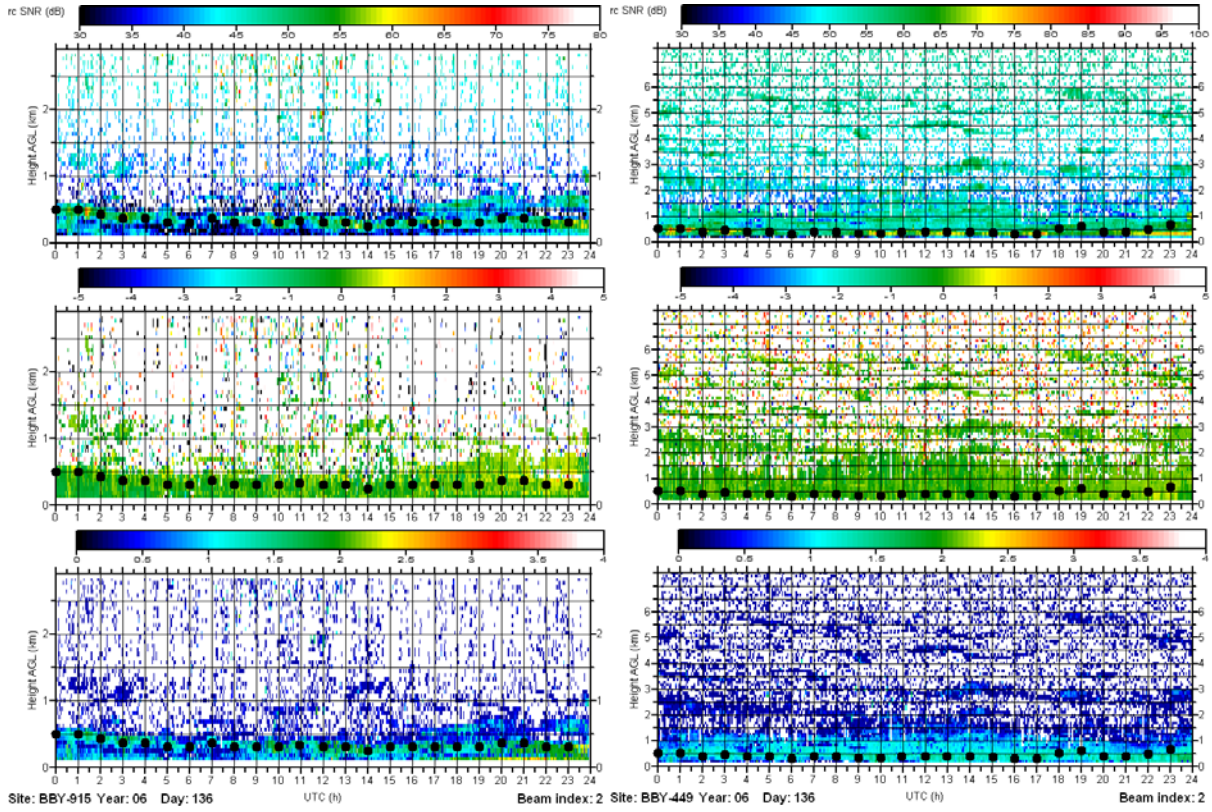

Figure 13. BBY-915 (left) and BBY-449 (right) time-height cross sections of vertical beam Doppler spectral moments for Julian day 136. Top panel: range-corrected SNR; middle panel: vertical velocity; lower panel: Doppler spectral width. The black dots denote BLD estimations produced by the automated algorithm.

Figure 14 is a scatterplot comparison of the BLD estimations for the entire analysis period when both profilers detected a BLD. Statistical results are shown in the upper right hand corner of the figure. The number of BLD estimations provided by the BBY-449 (1307) is greater than the number of BLD estimations provided by the BBY-915 (969). The first reason for this difference is the BBY-449's greater sensitivity to atmospheric turbulence, as demonstrated by Fig. 11. The second reason is attributable to the first and is the greater altitude coverage provided by the BBY-449, which gives the automated algorithm more data with which to determine the BLD. The air above the marine boundary layer along the West Coast of the U.S. is particularly difficult for the BBY-915 to observe because it is very dry and the wavelength is comparatively smaller (versus the BBY-449) to the inner scale of turbulence. The scatterplot also shows that there were a number of occasions when the BLDs measured by the BBY-915 were below the BLDs measured by the BBY-449. This behavior occurred approximately 15% of the time and when the boundary layers were shallow, which gave the BBY-915 two advantages because of its increased vertical resolution and lower minimum detectable range as compared to the BBY-449 (see Table 1).

For the 449-MHz wind profiler and RASS at GLA, we performed the same analysis with the Doppler spectral moments using the automated

algorithm and compared the results with BLD estimations derived from profiles of the virtual potential temperature, θ_v, measured by the GLA RASS. The RASS BLD estimates were determined by computing the vertical gradient of θ_v and then searching upward in the RASS profiles for the first altitude where the vertical gradient of θ_v fell below 0.3 ^{o}C km^{-1}. The altitude of the lower bound used in the gradient calculation was estimated to be the BLD. Figure 15 shows the BLD estimations for two days derived using the RASS θ_v profiles. Figure 16 compares the BLD estimations based on the two methods used for the same two days.

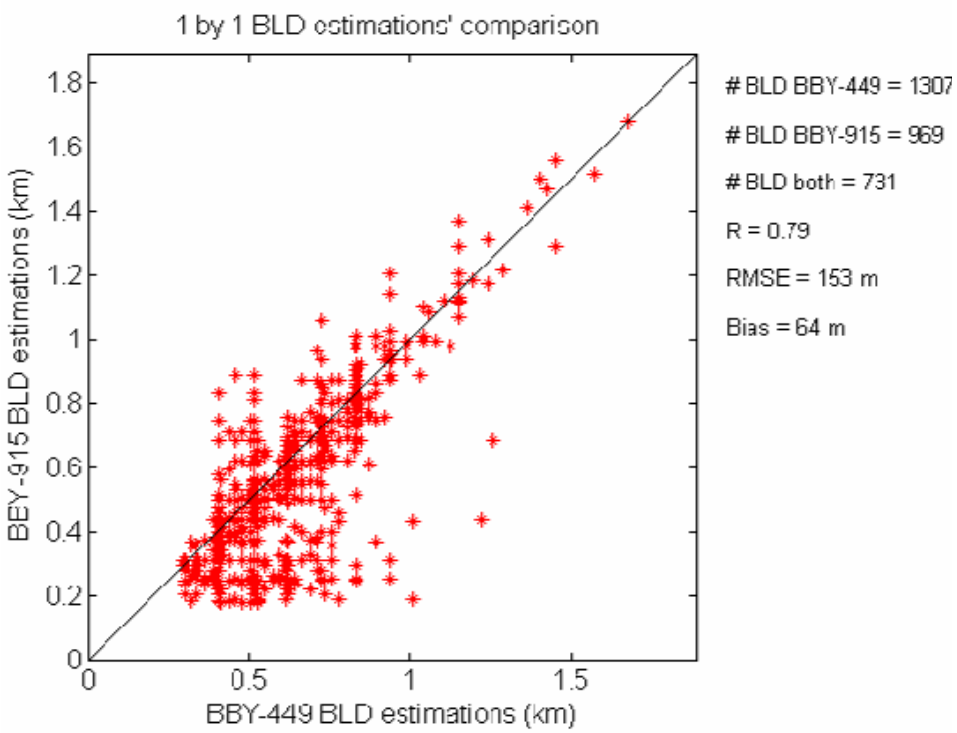

Figure 14. A scatterplot of boundary-layer depth (BLD) estimations by the BBY-449 and BBY-915 wind profilers.

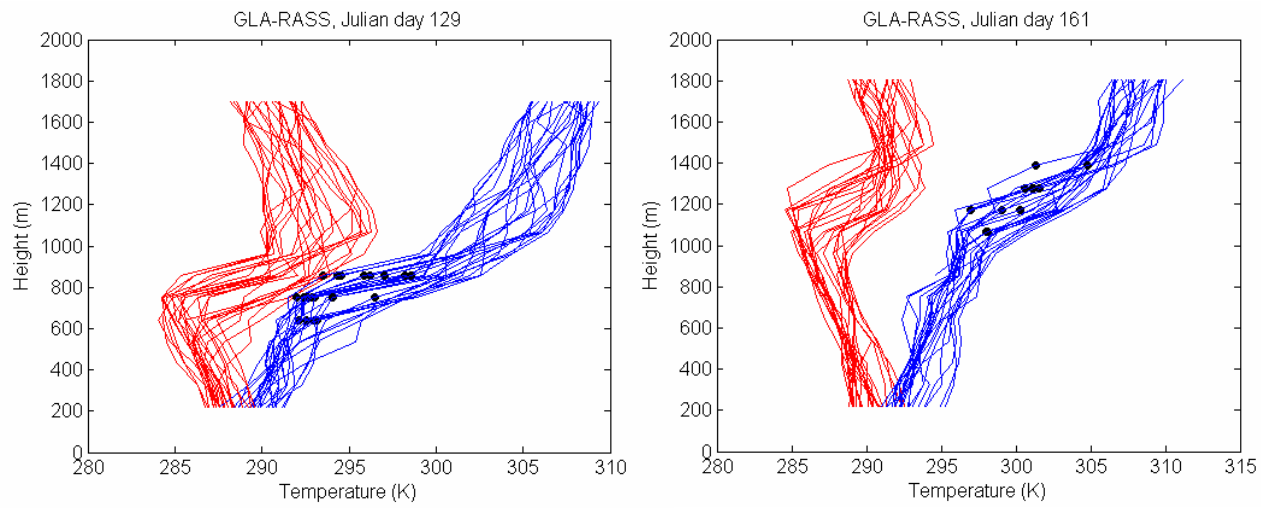

Figure 15. Hourly vertical profiles of virtual temperature (T_v; red) and virtual potential temperature (θ_v; blue) derived from RASS measurements at GLA on Julian day 129 (left) and Julian day 161 (right). The black dots denote the BLD estimations based on the gradient threshold described in the text.

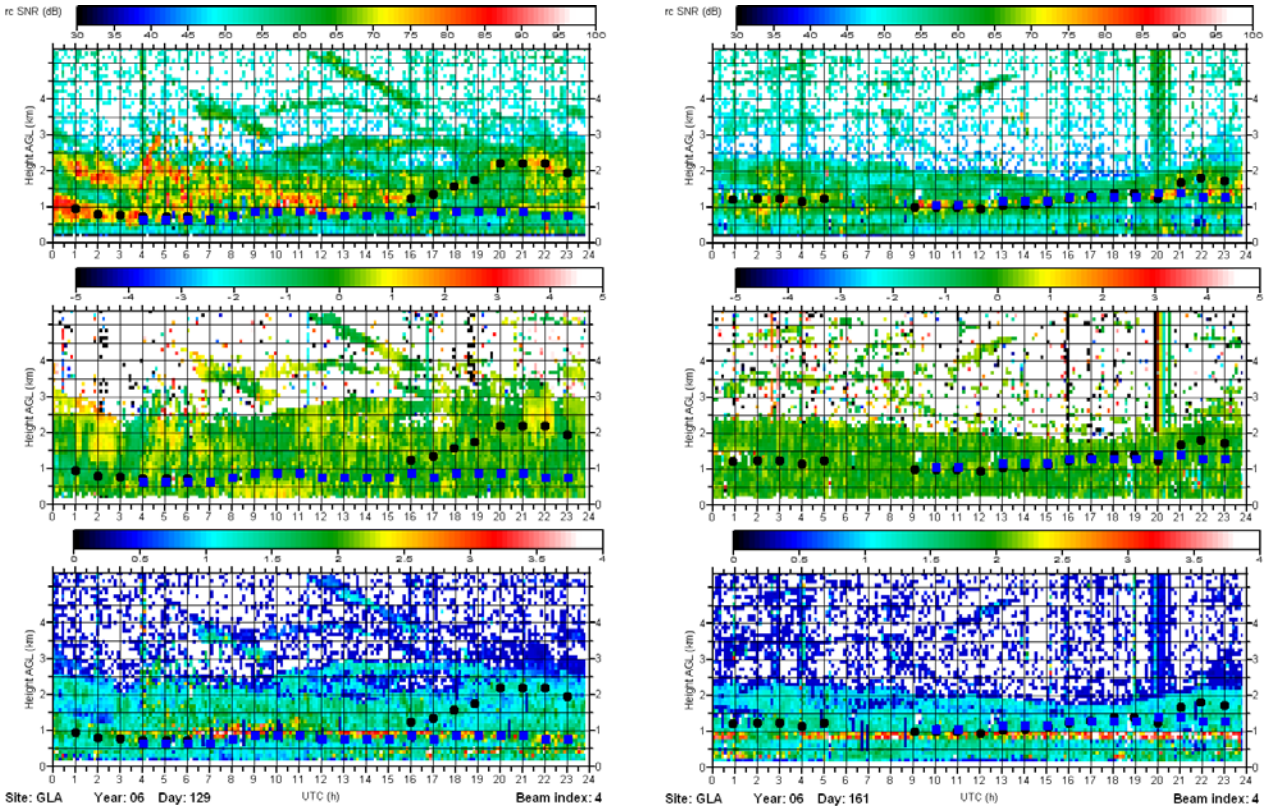

Figure 16. Time-height cross sections of vertical beam Doppler spectral moments measured by the GLA wind profiler for Julian days 129 (left) and 161 (right). Top panel: range-corrected SNR; middle panel: vertical velocity; lower panel: Doppler spectral width. The black dots denote BLD estimations produced by the automated algorithm and the blue dots denote BLD estimations from the virtual potential temperature profiles measured by the RASS.

By examining the entire dataset we determined that the 449-MHz RASS data provides an excellent method for determining the depth of the marine inversion, except for very stable marine boundary layers, where the inversion extends below the minimum detectable range of the wind profiler. When the wind profiler automated BLD estimation detected the altitude of the marine inversion and its estimate agreed with the RASS estimate, RASS data usually indicated a stable stratification below the inversion. We therefore don't know if a turbulent boundary layer existed. In many cases (e.g., Julian day 129) the BLD estimations obtained by the automated algorithm were above the inversion detected by the RASS. Figure 17 compares the BLDs produced by the two estimation methods.

Since neither method worked well for the very stable boundary layers encountered at GLA, we tried a third approach following Vogelezang and Holstang (1996), who proposed a bulk Richardson number for the stable boundary layer. In this approach the Richardson number is computed as:

$$R_b = (z - z_l)\left(\frac{g}{\overline{\theta}}\right)\frac{[\theta(z) - \theta_l]}{[U(z) - U_l]^2} \qquad (1)$$

where z is the top of the layer being considered and z_l is the bottom; $\overline{\theta}$ is the layer mean potential temperature; $\theta(z)$ is the potential temperature at z; θ_l is the potential temperature at the bottom of the layer; U(z) is the mean wind speed at z; U_l is the mean wind speed at the bottom of the layer.

In order to compute R_b using Eq. (1), surface measurements collected by meteorological sensors mounted on a 10-m tower collocated with the wind profiler and RASS at GLA were used together with the wind and temperature hourly profiles determined by the RASS-wind profiler

system. The R_b profile was then compared to a critical value that we choose to be equal to 0.3, in agreement with Vogelezang and Holstang (1996). Beginning with the level closest to the surface and searching upward, the top of the boundary layer was assumed to be the first height where R_b exceeded the critical value. Other methods have been proposed, although for the very stable boundary layer a definable depth is often difficult to determine (Vickers and Mahrt, 2004).

The results of the GLA RASS θ_v-gradient and R_b techniques were compared to the BLD estimations from the BBY-915 and BBY-449 wind profiler measurements. For both techniques scatterplots (not shown) were similar to the one presented for GLA in Fig. 17.

Neither wind profiler technology is ideally suited to measuring the shallow marine boundary layers that often exist along the U.S. West Coast under onshore flow conditions because of insufficient vertical resolution and minimum detectable range. For deeper marine boundary layers or for boundary layers that have more of a continental influence, the 449-MHz RASS provides the most unambiguous depiction of the capping inversion defining the boundary-layer depth. Because 449-MHz RASS outperformed 915-MHz RASS in terms of altitude coverage and data quality, the 449-MHz profiler makes a slightly better, suboptimal choice for detecting and monitoring coastal boundary-layer depth. A much more suitable technology for this application is sodar, which is currently being used operationally, for example, to monitor coastal boundary-layer depth at the San Francisco Airport.

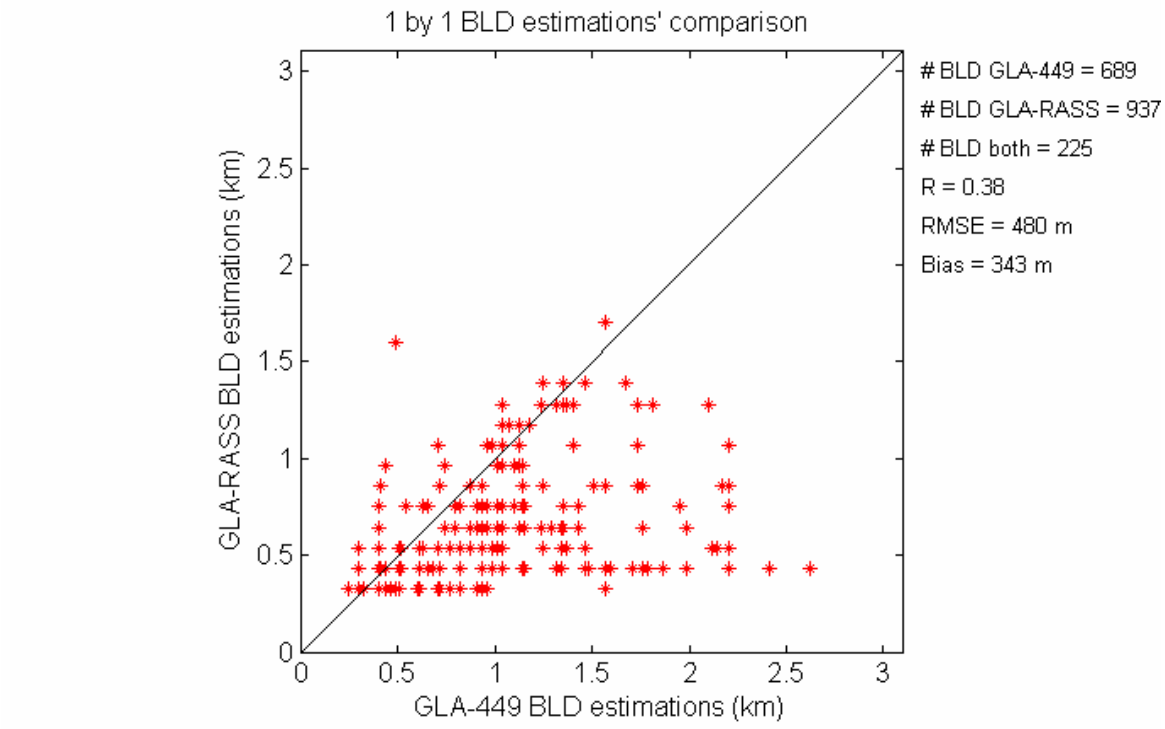

Figure 17. Scatterplot comparing the BLD estimates provided by GLA-449 using the automated algorithm (horizontal axis) and using the RASS θ_v gradients (vertical axis).

5. OTHER NEW PROFILER APPLICATIONS

Aside from the various applications discussed in Section 4, there have been a couple of other more recent wind profiler applications developed by scientists at ESRL. One of these is a computation of the bulk upslope water vapor flux as a means to document moisture transport up the windward slopes of terrain. This experimental product was based on four winters of analysis (Neiman et al., 2002) and combines information on storm forcing (winds aloft) measured by coastal wind profilers and the fuel (integrated water vapor measured by collocated Global Positioning System (GPS) receivers. During the winter of 2006-2007, the flux product was tested at several sites in California. An example is shown in Fig. 18. Note that the bulk flux measured at the coast is well correlated with rainfall rates in the nearby, downwind mountains. This real-time product is updated hourly on the Internet and could potentially become a useful aid for predicting and assessing precipitation amounts in areas where orographically enhanced precipitation is a concern.

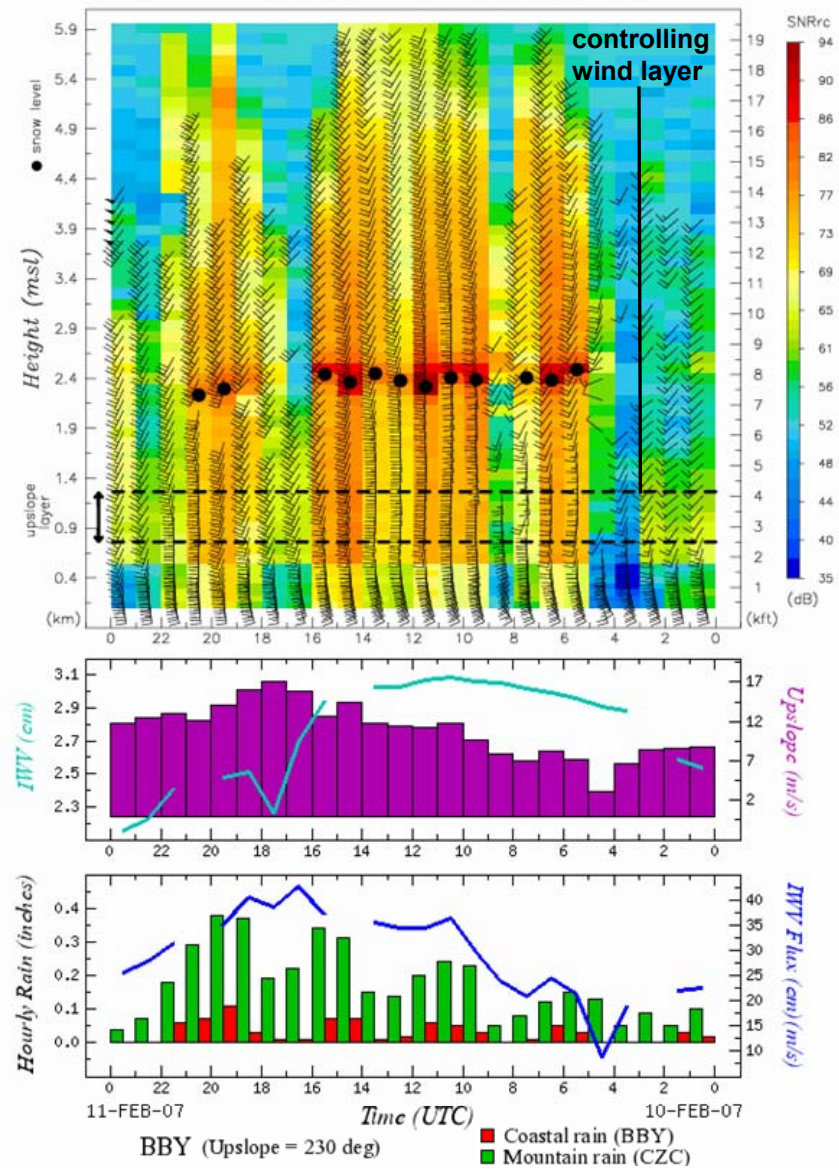

Figure 18. An example of the NOAA/ESRL water vapor transport tool. Hourly upslope flow in the controlling wind layer measured by the wind profiler at the coast (purple bars) is multiplied by integrated water vapor (IWV; cyan curve) measured by a collocated GPS receiver. The resulting IWV flux (dark blue curve) is well correlated with the coastal mountain rainfall measured downstream (green bars).

The second recently developed profiler application is a wind profiler-based trajectory tool (White et al., 2006). This trajectory tool differs from other trajectory tools because it uses only the horizontal winds measured by wind profiler networks to calculate the trajectories. No model physics or parameterizations are employed. A one-over-distance-squared weighting to the profiler locations is applied at each hourly position of the trajectory in order to calculate the next hourly position. Because the tool neglects vertical motion, the profiler trajectories calculated by this method do not adhere to mass balance considerations and, therefore, may differ substantially from trajectories based on full three-dimensional models. However, increased time resolution of the wind profiler observations (hourly versus twice daily for the operational sounding network that upon which most model-based trajectory programs are based) and continuity of the data, especially during active weather patterns, provide more important benefits for the trajectory calculations (White et al., 2006).

The profiler-based trajectories have been used in post-experiment analysis studies related to the 1995 and 1999 Southern Oxidants Studies (Banta et al., 1998), the 2000 Central California Ozone Study (CCOS), the Texas Air Quality Study (Banta et al., 2005) and more recently for the 2002 New England Air Quality Study (Darby et al., 2007) and the 2004 International Consortium for Atmospheric Research on Transport and Transformation filed study (ICARTT-04; Fisher et al., 2006; Millet et al., 2006, White et al., 2006; Williams et al., 2007). For the first time, the profiler trajectory tool was available on the Internet in real time for the 2005-2006 Texas air quality study (TEXAQS-II).

Figure 19 shows an example of forward trajectories from August 2-3, 2000 (during the CCOS experiment). Note how the low-level trajectories differ substantially from the upper-level trajectories, a pattern which is not uncommon in California during the summertime because of the flows associated with the marine boundary layer and the mean position of the Pacific ridge.

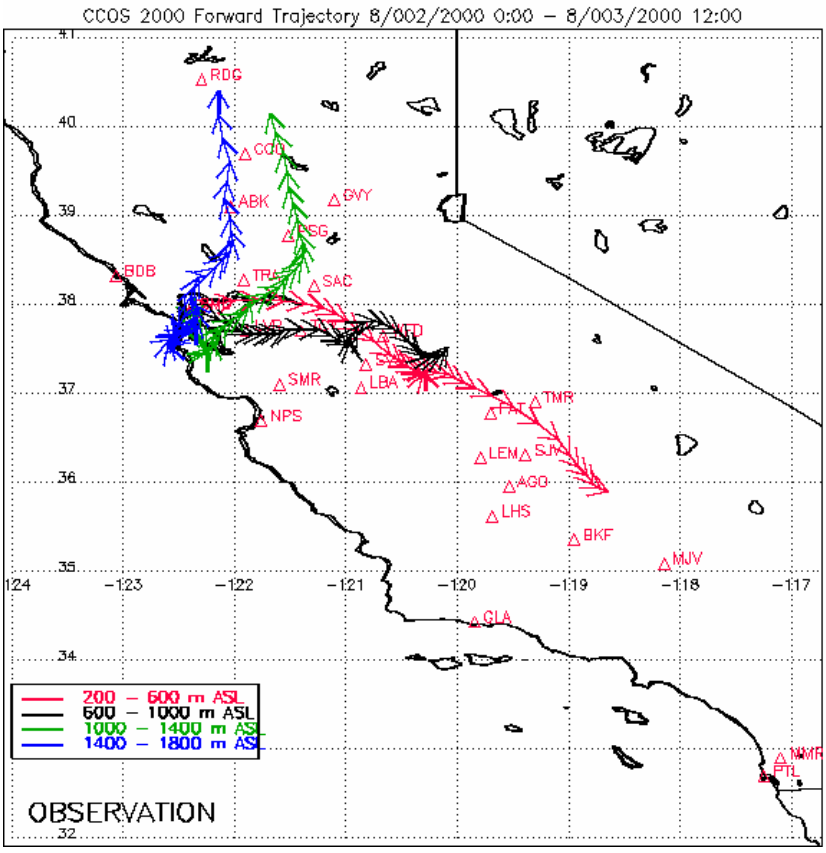

Figure 19. Sample forward trajectories (8/2/00 00:00 UTC to 8/3/00 12:00 UTC) produced from the NOAA wind profiler trajectory tool. The colors indicate altitude range of the wind profiler data used to calculate the trajectory as indicated by the key. The red triangles with three-letter labels denote the profiler locations.

6. SUMMARY AND DISCUSSION

Both wind profilers performed admirably during the technology evaluation, so with respect to their ability to provide continuous data throughout all seasons, there was not an advantage to using either technology. In addition, the evaluation was not long enough (11 months) to determine the long-term operating sustainability of either technology.

For wind profiling, the primary advantage of the ¼-scale 449-MHz wind profiler was extended altitude coverage (more than three times that of the 915-MHz wind profiler). This coverage is important for providing wind data for assimilation into numerical models and because it fills the gap between the surface, where relatively dense observing networks exist, and roughly 500 mb, where there is an increasing amount of automated aircraft measurements available. The analyses showed that the 449-MHz profiler's minimum detectable altitude was barely sufficient to capture important, shallow coastal weather phenomena such as gap flow. The increased sensitivity of the 449-MHz frequency to scattering from atmospheric turbulence relative to its sensitivity to scattering from hydrometeors meant that the 449-MHz wind profiler did not perform as well as the 915-MHz wind profiler for snow-level detection. However, the small number of cases for which this was true combined with the light rainfall that accompanied these events, indicated that for hydrometeorologically significant rainfall events, the 449-MHz wind profiler's performance in detecting the snow level was sufficient.

Again for wind profiling, the primary advantage of the 915-MHz wind profiler was minimum altitude coverage and vertical resolution. The 915-MHz profiler detects winds at a lower minimum altitude (110 m vs. 185 m). This increased low altitude coverage and enhanced vertical resolution allowed the 915-MHz profiler to better resolve the wind jet associated with gap flow. In addition, the enhanced vertical resolution combined with the absence of clear-air turbulence signals during precipitation meant that the 915-MHz wind profiler did a better job detecting the snow level, especially for lower altitude snow levels and in light precipitation events.

For temperature profiling via the RASS technique, it was clear that the 449-MHz RASS outperformed the 915-MHz RASS both in terms of maximum altitude coverage and data quality. The RASS profiles provide a superior method for detecting the inversion capping the turbulent coastal marine boundary layer as compared to the automated algorithm that was developed for detecting the depth of the convective planetary boundary layer (Bianco and Wilczak, 2002). For more stable boundary layers that are shallower than the minimum detectable range of the RASS or where the inversion extends to the surface, there does not appear to be an optimal way to measure the depth of the coastal marine boundary layer using either wind profiler technology. For the latter case, research has shown that there often is not a robust definition of boundary-layer depth. For the very shallow coastal marine boundary layers that can exist along the entire West Coast, or in the Gulf of Maine for example, sodar is perhaps the best possible technology to use (e.g., White et al., 1991). For locations where the depth and strength of the boundary layer are of primary importance, a sodar operating in conjunction with a wind profiling radar would create a powerful tool. At the time of this report, two sodars designed, built, and installed by ESRL were a critical component of the San Francisco Airport Marine Stratus Forecast System (Ivaldi et al., 2006).

The 449-MHz and 915 MHz wind profiler technologies are both commercially available. The 449-MHz wind profiler with RASS is approximately twice as expensive as the 915-MHz wind profiler with RASS. In addition the estimated annual expense of operating and maintaining a 449 MHz wind profiler is about twice the amount of operating and maintaining a 915 MHz wind profiler. These costs are based on prices and estimates provided by Vaisala, Inc., using the General Services Administration price schedule.

Perhaps the most serious challenge with respect to making either technology operationally viable is frequency security. Here the 449-MHz wind profiler has a clear advantage because the National Telecommunications and Information Administration has allocated the 448-450 MHz frequency band to wind profilers and amateur radio operators, although the Military is considered the primary operator in this frequency band. The 915-MHz profiler operates in the crowded band from 902-928 MHz that has been allocated to Instrumentation, Science, and Medicine. Even though NOAA has a Stage-three license to operate wind profilers in this band, the radio frequency interference (RFI) that exists today already is limiting the locations where 915-MHz

wind profilers can be deployed practically, and the problem is forecast to get even worse in the future.

Finally, it may make perfect logistical sense for all of NOAA's profilers to operate at the same frequency. In this case the 449-MHz wind profiler technology would be preferred for coastal applications because 449 MHz will be the new operating frequency of the NOAA Profiler Network (NPN) wind profilers located primarily in the central part of the U.S. However, unless the new NPN technology is able to provide higher resolution profile data and improved minimum detectable range than its predecessor, then this technology will not be suitable for coastal weather applications. Ultimately, what may be required is a scalable wind profiler technology, one that will allow the meteorological forecast problems for which the observed data are intended to help solve dictate how the technology is optimized for a particular region. Clearly, technology assessments such as this one funded by the Integrated Ocean Observing System are necessary before adopting a "one-size-fits all" strategy for future enhancements to the Nation's coastal observing system.

7. REFERENCES

Banta, R. M., et al., 1998: Daytime buildup and nighttime transport of urban ozone in the boundary layer during a stagnation episode. *J. Geophys. Res.*, **103**, 22,519-22,544.

Banta, R. M., C. J. Senff, J. Nielsen-Gammon, L. S. Darby, T. B. Ryerson, R. J. Alvarez, S. P. Sandberg, E. J. Williams, and M. Trainer, 2005: A bad air day in Houston. *Bull. Am. Meteorol. Soc*., **86**, 657-669.

Batton, L.J., 1973: Radar Observations of the Atmosphere. University of Chicago Press, Chicago, IL, 323 pp.

Bianco, L., and J. M. Wilczak, 2002: Convective boundary layer mixing depth: Improved measurement by Doppler radar wind profiler using fuzzy logic. *J. Atmos. Oceanic Technol*., **19**, 1745-1758.

Bianco, L., J. M. Wilczak, and A. B. White, 2007: Convective boundary layer depth estimation from wind profilers: statistical comparison between an automated algorithm and expert estimations, *J. Atmos. Oceanic Technol*., submitted.

Bond, N.A., and P.J. Stabeno, 1998: Analysis of surface winds in Shelikof Strait, Alaska, using moored buoy observations. *Wea. Forecasting*, **13**, 547-559.

Carter, D. A., K. S. Gage, W. L. Ecklund, W. M. Angevine, P. E. Johnston, A. C. Riddle, J. Wilson, and C. R. Williams, 1995: Developments in UHF lower tropospheric wind profiling at NOAA's Aeronomy Laboratory. *Radio Sci.*, **30**, 977-1001.

Chadwick, R.B., 1988: The Wind Profiler Demonstration Network. Extended Abstracts, *Symp. on Lower Tropospheric Profiling: Needs and Technologies*, 31 May-3 June 1988, Boulder, CO. Amer. Meteorol. Soc., Boston, 109-110.

Fisher, E., A. Pszenny, W. Keene, J. Maben, A. Smith, J. Stutz, R. Talbot, C. Senff, and A. White, 2006: Nitric acid phase partitioning and cycling in the New England coastal atmosphere. *J. Geophys. Res.*, **111**, D23S09, doi:10.1029/2006JD007328.

Colle B. A., and C. F. Mass, 2000: High-resolution observations and numerical simulations of easterly gap flow through the Strait of Juan de Fuca on 9-10 December 1995. *Mon. Wea. Rev.*, **128**, 2398-2422.

Colle, B.A., K.A. Loescher, G.S. Young, and N.S. Winstead, 2006: Climatology of barrier jets along the Alaskan coast, Part II: Large-scale and sounding composites. *Mon. Wea. Rev*., **134**, 454-477.

Darby, L. S., et al., 2007: Ozone differences between near-coastal and offshore sites in New England: Role of meteorology. *J. Geophys. Res.*, **112**, D16S91, doi:10.1029/2007JD008446.

Colman, B.R., and C.F. Dierking, 1992: The Taku wind of southeast Alaska: Its identification and prediction. *Wea. Forecasting*, **7**, 49-64.

Ghebrebrhan, O., 1990: Full decoding of truncated ranges for ST/MST radar applications. *IEEE Trans. Geosci. Remote Sens*., **28**, 14-18.

Gilliam, H., 1970: Weather of the San Francisco Bay Region. University of California Press, 72 pp.

Holets, S., and R.N. Swanson, 1981: High-inversion fog episodes in central California. *J. Appl. Meteor*., **20**, 890-899.

Holets S., and R. N. Swanson, 1981: High-inversion fog episodes in central California. *J. Appl. Meteor.*, **20**, 890-899.

Ivaldi, C., D. Clark, and D. Reynolds, 2006: Upgrade and technology transfer of the San Francisco Marine Stratus Forecast System to the National Weather Service. Preprint Vol., *12th Conf. on Aviation, Range, and Aerospace Meteorology*, 30 Jan.–2 Feb., 2006, Atlanta, GA, AMS, Boston.

Jackson, P.L., and D.G. Steyn, 1994: Gap winds in a fjord. Part I: Observations and numerical simulation. *Mon. Wea. Rev.*, **122**, 2645-2665.

Loescher, K.A., G.S. Young, B.A. Colle, and N.S. Winstead, 2006: Climatology of barrier jets along the Alaskan coast, Part I: Spatial and temporal distributions. *Mon. Wea. Rev.*, **134**, 437-453.

Mass, C.F., S. Businger, M.D. Albright, and Z.A. Tucker, 1995: A windstorm in the lee of a gap in a coastal mountain barrier. *Mon. Wea. Rev.*, **123**, 315-331.

Millet, D. B., et al., 2006: Chemical characteristics of North American surface layer outflow: Insights from Chebogue Point, Nova Scotia. *J. Geophys. Res.*, **111**, D23S53, doi:10.1029/2006JD007287.

Neiman, P.J., F.M. Ralph, A.B. White, D.A. Kingsmill, and P.O.G. Persson, 2002: The statistical relationship between upslope flow and rainfall in California's coastal mountains: Observations during CALJET. *Mon. Wea. Rev.*, **130**, 1468-1492.

Neiman, P.J., F.M. Ralph, A.B. White, D.D. Parrish, J.S. Holloway, and D.L. Bartels, 2006: A Multiwinter analysis of channeled flow through a prominent gap along the northern California Coast during CALJET and PACJET. *Mon. Wea. Rev.*, **134**, 1815-1841.

Sharp J. M., 2002: Columbia Gorge gap flow. *Bull. Amer. Meteor. Soc.*, **83**, 1757–1762.

Underwood, S.J., G.P. Ellrod, and A.L. Kuhnert, 2004: A multiple-case analysis of nocturnal radiation-fog development in the Central Valley of California utilizing the GOES nighttime fog product. *J. Appl. Meteor.*, **43**, 297-311.

Vickers, D., and L. Mahrt, 2004: Evaluating formulations of stable boundary layer height. *J. Appl. Meteor.*, **43**, 1736-1749.

Vogelezang D. H. P., and A. A. M. Holtslag, 1996: Evaluation and model impacts of alternative boundary-layer height formulations, *Bound.-Layer Meteor.*, **81**, 245-269.

Weber, B.L., D.B. Wuertz, D.C. Welsh, and R. McPeek, 1993: Quality controls for profiler measurements of winds and RASS temperatures. *J. Atmos. Oceanic Technol.*, **10**, 452-464.

White, A.B., C.W. Fairall, and D.W. Thomson, 1991: Radar observations of humidity variability in and above the marine atmospheric boundary layer. *J. Atmos. Oceanic Technol.*, **8**, 639-658.

White, A.B., D.J. Gottas, E. Strem, F.M. Ralph, and P.J. Neiman, 2002: An automated bright-band height detection algorithm for use with Doppler radar vertical spectral moments. *J. Atmos. Oceanic Technol.*, **19**, 687-697.

White, A. B., C. J. Senff, A. N. Keane, L. S. Darby, I. V. Djalalova, D. C. Ruffieux, D. E. White, B. J. Williams, and A. H. Goldstein, 2006: A wind profiler trajectory tool for air quality transport applications, *J. Geophys. Res.*, **111**, D23S23, doi:10.1029/2006JD007475.

White, A. B., L. S. Darby, C. J. Senff, C. W. King, R. M. Banta, J. Koermer, J. M. Wilczak, P. J. Neiman, W. M. Angevine, and R. Talbot, 2007: Comparing the impact of meteorological variability on surface ozone during the NEAQS (2002) and ICARTT (2004) field campaigns. *J. Geophys. Res.*, **112**, D10S14, doi:10.1029/2006JD007590.

Wilczak, J.M., R.G. Strauch, F.M. Ralph, B.L. Weber, D.A. Merritt, J.R. Jordan, D.E. Wolfe, L.K. Lewis, D.B. Wuertz, and J.E. Gaynor, 1995: Contamination of wind profiler data by migrating birds: Characteristics of corrupted data and potential solutions. *J. Atmos. Oceanic Technol.*, **12**, 449-467.

Williams, et al., 2007: Chemical speciation of organic aerosol during the International Consortium for Atmospheric Research on Transport and Transformation 2004: Results from in situ measurements. *J. Geophys. Res.*, **112**, D10S26, doi:10.1029/2006JD007601.

Wolfe D. E., B. L. Weber, T. L. Wilfong, D. C. Welsh, D. B. Wuertz, and D. A. Merritt, 2001: An advanced signal processing system for radar wind profilers. Preprint Vol., *11th Symp. on Meteorological Observations and Instrumentation*, Albuquerque, NM, Amer. Meteor. Soc., 339–344.